Simulations of subatomic many-body physics on a quantum frequency processor

Hsuan-Hao Lu,[1,*] Natalie Klco,[2,*] Joseph M. Lukens,[3] Titus D. Morris,[4,3] Aaina Bansal,[5] Andreas Ekström,[6] Gaute Hagen,[4,5] Thomas Papenbrock,[5,4] Andrew M. Weiner,[1] Martin J. Savage,[2] and Pavel Lougovski[3,†]

[1]*School of Electrical and Computer Engineering and Purdue Quantum Science and Engineering Institute, Purdue University, West Lafayette, Indiana 47907, USA*

[2]*Institute for Nuclear Theory, University of Washington, Seattle, Washington 98195-1550, USA*

[3]*Quantum Information Science Group, Computational Sciences and Engineering Division, Oak Ridge National Laboratory, Oak Ridge, Tennessee 37831, USA*

[4]*Physics Division, Oak Ridge National Laboratory, Oak Ridge, Tennessee 37831, USA*

[5]*Department of Physics and Astronomy, University of Tennessee, Knoxville, Tennessee 37996, USA*

[6]*Department of Physics, Chalmers University of Technology, SE-412 96 Göteborg, Sweden*

(Received 5 February 2019; published 15 July 2019)

Simulating complex many-body quantum phenomena is a major scientific impetus behind the development of quantum computing, and a range of technologies are being explored to address such systems. We present the results of the largest photonics-based simulation to date, applied in the context of subatomic physics. Using an all-optical quantum frequency processor, the ground-state energies of light nuclei including the triton (^{3}H), ^{3}He, and the alpha particle (^{4}He) are computed. Complementing these calculations and utilizing a 68-dimensional Hilbert space, our photonic simulator is used to perform subnucleon calculations of the two- and three-body forces between heavy mesons in the Schwinger model. This work is a first step in simulating subatomic many-body physics on quantum frequency processors—augmenting classical computations that bridge scales from quarks to nuclei.

DOI: 10.1103/PhysRevA.100.012320

I. INTRODUCTION

Photonics is at the forefront of experimental quantum computing, as evidenced by pioneering demonstrations of the variational quantum eigensolver (VQE) algorithm [1–3], of molecular vibronic spectra and dynamics simulations [4,5], and of experimental Hamiltonian learning [6]. It offers a versatile platform to process quantum information with low noise in a multitude of encodings, ranging from spatial or polarization degrees of freedom [7,8] to temporal modes [9,10]. Rapid progress in integrating optical components on-chip [11–13] is paving the way to large-scale spatial-encoding-based photonic quantum processors. Other encodings, however, also provide a path to scalable quantum architectures. For example, frequency encoding—routinely used in fiber optics to multiplex information transmission and processing—has been adapted for scalable quantum computing [14]. A single fiber can support thousands of frequency modes that can be manipulated in a massively parallel fashion at the single-photon level. This particular framework for photonic quantum computing relies on qubits encoded in narrow frequency bins, where quantum gates are based on standard telecommunication equipment: electro-optic phase modulators (EOMs) and Fourier-transform pulse shapers [14]. A variety of basic quantum functionalities have recently been demonstrated experimentally in this approach in the form of a quantum frequency processor (QFP) [15–17].

Solving quantum many-body systems, whose resource requirements scale exponentially with the number of particles, is an area in which quantum devices are anticipated to provide a quantum advantage. Recently, quantum many-body problems in chemistry, condensed matter, and subatomic physics have been addressed with quantum computing using two-to-six superconducting qubits, for example, Refs. [18–22], and up to tens of trapped ions, for example, Refs. [23–25].

A major goal in nuclear physics research is to tie the effective field theory (EFT) descriptions of nuclear matter and heavy nuclei to their microscopic origin, quantum chromodynamics (QCD), through numerical calculations with lattice QCD. Important steps are being taken toward this objective [26–37]. A hierarchy of EFT models [38–40] is used to describe heavier nuclei [41–44], and lattice QCD calculations have been used to constrain EFT parameters over a range of unphysical quark masses [28,29,34–36]. However, such microscopic descriptions are computationally challenging for all but the lightest nuclei and hypernuclei [26,27,29–33] due to signal-to-noise problems [45–49]. Augmenting classical calculations with their quantum counterparts [50–53] offers an analogous roadmap for quantum-enabled subatomic physics, as depicted in Fig. 1. At the EFT level, a subatomic system can be simulated as a collection of nucleons with EFT parameters input from experimental data or from *ab initio*, Minkowski-space quantum simulations of lattice QCD. In this article, we take the first steps to meeting this "Grand Challenge."

*These authors contributed equally to this work.
†To whom correspondence should be addressed; lougovskip@ornl.gov

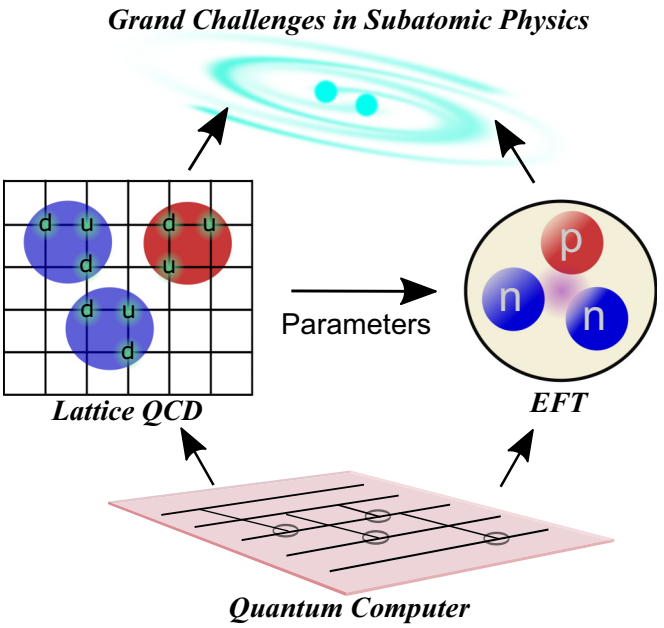

FIG. 1. Quantum simulation for subatomic physics. Ideally, quantum simulation applied to both QCD (left side) and EFT (right side) will enable high-precision predictions of static and dynamic properties of nuclei and nuclear matter. EFT parameters may be determined from experiment or by a complementary program of classical and quantum simulation.

We report the application of a QFP to many-body subatomic systems. With Hilbert spaces of up to 68 dimensions, this work may represent the largest simulation of nuclei and lattice field theories on a photonic device to date. Using an EFT description, we experimentally implement the VQE algorithm to calculate the binding energies of ^{3}H, ^{3}He, and ^{4}He. Further, we employ VQE to determine the effective interaction potential between composite particles directly from an underlying lattice quantum gauge field theory—the Schwinger model. This serves as an important demonstration of how EFTs themselves can be both implemented and determined from first principles by means of quantum simulations.

II. QUANTUM FREQUENCY PROCESSOR (QFP)

For implementing quantum simulations, we utilize our previously developed QFP: a photonic device that processes quantum information encoded in equispaced narrow-band frequency bins, described by operators $c_n^\dagger$ (c_n) for $n \in \mathbb{Z}$ that create (annihilate) a photon in a mode centered at $\omega_n = \omega_0 + n\Delta\omega$, where $\Delta\omega$ is the frequency-bin spacing and ω_0 is an offset [14,54]. An arbitrary, unitary mode transformation matrix V can be implemented on QFP by interleaving pulse shapers and EOMs [14], and recent experiments have demonstrated high-fidelity single-qubit [15,16] and two-qubit [17] gates.

Figure 2 shows the experimental setup for our all-optical QFP. The input state preparation, frequency operations, and final energy measurements can all be realized with off-the-shelf fiber-optic components, including EOMs (EOSpace), pulse shapers (Finisar), and an optical spectrum analyzer (OSA, Yokogawa). The capability of transmitting optical information within a single-mode fiber from generation to detection facilitates parallel computations in a low-noise fashion.

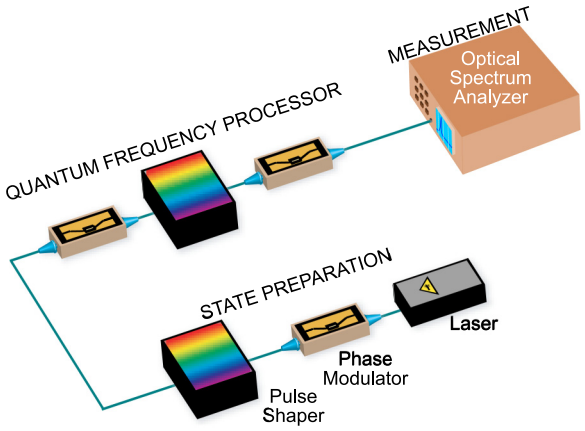

FIG. 2. Experimental setup including our all-optical quantum frequency processor.

As detailed in the Methods section, for many-body Hamiltonians projected onto single-particle subspaces a variational wave function can be mapped onto a mode-entangled state of a single photon so that the state preparation procedure in the VQE algorithm amounts to coherent frequency comb generation. However, more complicated (e.g., multiphoton) entangled photonic states could be employed as well, modifying only the "state preparation" portion of the apparatus in Fig. 2. By working with multiple photons in the QFP, qubit degrees of freedom can be identified with photon occupations of frequency-bin pairs. For example, ten frequency bins, discussed below, can be mapped onto five qubits with a five-photon input state. Such a mapping and the ability to implement a universal gate set endows the QFP with similar quantum capabilities and scaling as other digital quantum devices. Note that the QFP utilized in this work can in principle support the Hilbert space of up to 33 qubits [15,55]. Scaling this hardware to larger numbers of qubits will require further engineering in order to build multiple multiphoton sources and reduce loss in the system, which should ultimately enable a concrete quantum advantage over classical computing. This quantum advantage is not present in the single-photon methods employed in this work.

In this initial experiment, however, we focus on the simpler case of single-photon encoding for demonstrating the basic approach. The source we utilize for the state preparation is a wavelength-division multiplexing transmitter (Ortel) possessing four cw laser modules emitting single-tone optical signals at 192.0, 192.4, 192.8, and 193.2 THz. We combine all four signals with a fiber coupler and send them through an EOM driven at 25 GHz, which creates four parallel frequency combs at the output (each of which contains ∼10 frequency bins) with a total of 40 available comb lines. This allows us to implement up to eight parallel Hadamard gates (50:50 beamsplitters): two comb lines per gate plus four comb lines for guardbands (i.e., two gates per each ten-line subcomb) to prevent cross-contamination during the subsequent frequency beamsplitting operations (photons from one gate jumping over to an adjacent

gate during the calculation) [15]. We then choose the best five beamsplitters for the subsequent operation, excluding those with higher imbalance in reflectivity and transmissivity. Note that despite these calibration measures, we still observe the residual nonuniform performance across different gates stemming from the noise background of the input light source, and the optical path length change in the QFP due to temperature drifts in long-term measurements. Finally, filtering out extra input frequencies, as well as manipulating amplitude and phase for all five remaining frequency-bin pairs, is realized by a pulse shaper immediately following the comb generation.

III. MAPPING SYSTEMS ONTO THE QFP

In all quantum simulations here, our starting point is a second-quantized Hamiltonian $\mathcal{H}_{\rm SQ}$ which, depending on the problem, contains one-, two-, and three-particle terms written as products of fermionic creation and annihilation operators. Our goal for these Hamiltonians is to compute the smallest eigenvalue using the QFP hardware. A scalable path to this goal has been outlined in the literature in the form of the VQE algorithm [56]. There, each fermionic operator in $\mathcal{H}_{\rm SQ}$ is mapped onto a set of qubits such that fermionic commutation relationships are preserved. As a result $\mathcal{H}_{\rm SQ}$ is mapped onto $\tilde{\mathcal{H}}_{\rm SQ}$, which is a sum of strings of Pauli operators. Then quantum hardware is used to prepare a variational trial quantum state of qubits $|\Psi = \Psi(\theta_1, \ldots, \theta_M)\rangle$ in the form of a parameterized quantum circuit with M parameters. Subsequently, the expectation value of the Hamiltonian in the state $|\Psi\rangle$, $\langle\Psi|\tilde{\mathcal{H}}_{\rm SQ}|\Psi\rangle$ is computed by repeating the state preparation and energy measurement multiple times. A classical computer calculates the direction in the parameter space and new parameter values $\{\theta'_1, \ldots, \theta'_M\}$ that yield a lower energy value. The energy calculation is then repeated on quantum hardware with the updated trial state $|\Psi(\theta'_1, \ldots, \theta'_M)\rangle$ until a (local) minimum of the energy is obtained.

For all pre-error-corrected quantum hardware—of which the QFP is an example—the depth of the circuit that prepares and measures the variational state $|\Psi\rangle$ is limited by noise. This effectively limits the size of fermionic systems that can be simulated on existing devices. To extend quantum simulations to subatomic systems beyond the deuteron [20] and Schwinger models beyond two spatial lattice sites [21,23], we have recently proposed a preconditioning strategy [21] that transforms $\tilde{\mathcal{H}}_{\rm SQ}$ into block-diagonal form by projecting it onto eigenstates of operators that represent good quantum numbers (e.g., parity, momentum, total spin) for the system of interest. As a result, $\tilde{\mathcal{H}}_{\rm SQ} = \bigoplus_i \mathcal{H}_i$, where $\mathcal{H}_i$ can now be interpreted as single-particle Hamiltonians acting on smaller subspaces than the original Hilbert space corresponding to $\tilde{\mathcal{H}}_{\rm SQ}$. A Hamiltonian $\mathcal{H}_i$, specified by a $d\times d$ Hermitian matrix with elements h_{kl} in some basis, can be mapped onto a Hamiltonian $\mathcal{H}^i_{\rm QFP}$ that describes a frequency-bin multiport device implementable with the QFP:

$$\mathcal{H}^i_{\rm QFP} = \sum_{k=0}^{d-1} h_{kk} c_k^\dagger c_k + \sum_{\substack{k,\,l=0\\ k<l}}^{d-1} [h_{kl} c_k^\dagger c_l + h_{kl}^* c_l^\dagger c_k], \qquad (1)$$

where h_{kl} are the entries in $\mathcal{H}_i$. In this encoding, we have mapped the original Hamiltonian $\tilde{\mathcal{H}}_{\rm SQ}$ onto a set of single-particle systems defined by Eq. (1). To find ground-state energies of each single-particle Hamiltonian $\mathcal{H}_i$ we implement a variant of the VQE algorithm adapted for the QFP hardware. For the trial variational wave function $|\Psi\rangle$ we utilize an ansatz based on unitary coupled-cluster (UCC) theory [56]. The UCC wave function can be written as

$$|\Psi\rangle = \exp\left(\sum_{k=1}^{d-1} \theta_k [c_0^\dagger c_k - c_k^\dagger c_0]\right) |10\cdots0\rangle, \qquad (2)$$

where the state $|0\cdots1_k\cdots0\rangle$ denotes a single excitation (photon) in the frequency bin k and none in the remaining $d-1$. The operator exponent can be evaluated explicitly in this case, leading to the following $(d-1)$-parameter state:

$$|\Psi\rangle = \cos\phi\,|10\cdots0\rangle - \frac{\sin\phi}{\phi}\sum_{k=1}^{d-1}\theta_k|0\cdots1_k\cdots0\rangle, \qquad (3)$$

with $\phi = \sqrt{\sum_{k=1}^{d-1}\theta_k^2}$. In the context of the QFP, the UCC wave function $|\Psi\rangle$ represents a superposition of a single photon over d frequency bins.

With the Hamiltonian and UCC wave function defined, we use our QFP to estimate the expectation value $\langle\mathcal{H}^i_{\rm QFP}\rangle = {\rm Tr}[|\Psi\rangle\langle\Psi|\mathcal{H}^i_{\rm QFP}]$ for given parameter values $\{\theta_k\}$, by first preparing $|\Psi\rangle$ and experimentally reconstructing the elements of the single-particle density matrix $\rho_{kl} = (1/2)\langle\Psi|c_k^\dagger c_l + c_l^\dagger c_k|\Psi\rangle$. Measuring ρ_{kl} is equivalent to placing the state $|\Psi\rangle$ on a 50:50 beamsplitter implemented between frequency bins k and l, and recording the difference in the flux of detected particles in those modes immediately after the beamsplitter. Similarly, elements ρ_{kk} can be measured by preparing the state $|\Psi\rangle$ and measuring the photon flux in each mode k by using a photodetector. After repeating this process for all combinations of modes k and l, $\langle\mathcal{H}^i_{\rm QFP}\rangle = {\rm Tr}[\rho\mathcal{H}^i_{\rm QFP}] = \sum_{kl}\rho_{kl}h_{kl}$ can be estimated. Recent formulations of VQE, which use the current estimate of the energy $\langle\mathcal{H}^i_{\rm QFP}\rangle$ to generate parameter updates $\{\delta\theta_k\}$ via a gradient-based classical optimizer, generally require many evaluations of $\langle\mathcal{H}^i_{\rm QFP}\rangle$ to arrive at converged parameters. We instead use a method which merges the UCC ansatz with a many-body formalism called the anti-Hermitian contracted Schrödinger equation [57]. This allows us to approximate the gradient of parameters using the measured ρ_{kl} of each iteration [58] and arrive at convergence with significantly fewer evaluations of $\langle\mathcal{H}^i_{\rm QFP}\rangle$. For example, in the problems we explore here our method required ∼20 iterations to converge compared to ∼500 iterations when using the Broyden-Fletcher-Goldfarb-Shanno (BFGS) algorithm [59].

In practice, the measurement of the elements ρ_{kl} using the single-photon state $|\Psi\rangle$ as an input is equivalent to a measurement with a coherent frequency comb where the relative amplitude of each comb line is set to $\theta_k\sin\phi/\phi$ (for lines $k = 1, \ldots, d-1$) and $\cos\phi$ (for the line $k = 0$) with respect to a reference coherent-state amplitude α. Indeed, one can verify by a direct calculation that

$\langle\Psi_{\rm comb}|\mathcal{H}^i_{\rm QFP}|\Psi_{\rm comb}\rangle = |\alpha|^2\langle\Psi|\mathcal{H}^i_{\rm QFP}|\Psi\rangle$, where

$$|\Psi_{\rm comb}\rangle = |\alpha\cos\phi\rangle \otimes \left|\alpha e^{i\pi}\frac{\theta_1\sin\phi}{\phi}\right\rangle \otimes\cdots\otimes \left|\alpha e^{i\pi}\frac{\theta_{d-1}\sin\phi}{\phi}\right\rangle. \quad (4)$$

Moreover, the measurements of ρ_{kl} for nonoverlapping sets of indices k, l can be implemented in parallel, thus reducing the simulation time, as the QFP has an intrinsic ability to perform the same operation on different sets of modes in parallel. Previously, we implemented near-unity fidelity frequency-bin beamsplitters in parallel, with a theoretical predicted fidelity $\mathcal{F} = 0.9999$. Such Hadamard gates can be achieved by driving two EOMs with π-phase-shifted sinewaves at frequency $\Delta\omega$ (with maximum temporal phase modulation $\Theta = 0.8169$ rad) and applying a step function with π phase jump between the two computational modes on the central pulse shaper. The corresponding beamsplitter possesses 47.81% reflectivity $\mathcal{R}$ (mode-hopping probability) and 49.79% transmissivity $\mathcal{T}$ (probability of preserving frequency), with 2.4% of the photons scattered outside of the computational space.

Despite such high fidelity, the residual imbalance in $\mathcal{R}$ and $\mathcal{T}$ is undesirable, leading to higher error in calculation of the ρ_{kl} elements. Accordingly, in this work we further reduce the Hadamard gate's bias, achieving $\mathcal{R} = 48.7\%$ and $\mathcal{T} = 48.77\%$ (corresponding to a fidelity $\mathcal{F} = 0.999\,999$) by increasing Θ to 0.8283 rad on both EOMs, while the QFP's central pulse shaper remains unchanged.

After setting up the Hadamard gates, we utilize the first pulse shaper to equalize the amplitude across all ten input frequency bins. The relative spectral phase within every frequency pair is also fine-tuned until we find the in-phase condition as the reference—defined such that the lower (higher)-frequency bin obtains the maximum (minimum) optical power after the Hadamard operation. To compute ρ_{kl}, we manipulate the relative amplitude and phase of a frequency pair c_k and c_l, and record the optical power difference between two modes after the beam-splitting operation. To reconstruct the full density matrix, a total number of $d(d-1)/2$ beam-splitting operations is required in every iteration. Hence, the usage of five parallel beamsplitters (as well as the natural parallelization in pulse shapers and the OSA) reduces the required number of computations by a factor of 5 before updating the trial state for the next iteration.

IV. NUCLEAR STRUCTURE CALCULATIONS

Organizing principles rooted in the global symmetries of QCD have been successfully encoded in low-energy EFT frameworks describing nuclear forces, providing a systematically improvable approach to calculations of nuclei. At low resolution, i.e., at long wavelengths, details about the strong but short-ranged nuclear forces, or about QCD, are not revealed, and the lightest nuclei can be understood in terms of contact interactions of pairs and triplets of nucleons [38,60–63]. In our model, we employ a Hamiltonian at next-to-leading order (NLO) in pionless EFT and adjust its parameters to the S-wave effective range expansions and the deuteron binding energy; the strength of the three-body contact is adjusted to the triton binding energy. The Coulomb force between protons is also included. We employ a finite basis consisting of eigenstates of the spherical harmonic oscillator with energy spacing $\hbar\omega = 22$ MeV in a discrete variable representation [36,64], with the two- and three-body potentials acting only between states with excitation energies up to and including $2\hbar\omega$. This discretization maps nucleon fields onto annihilation operators with an interaction-momentum cutoff of 337 MeV. Next, we project this second-quantized Hamiltonian $\mathcal{H}_{\rm SQ}$ onto Hilbert spaces with spin and parity of $J^\pi = 0^+$ for ^{4}He and $J^\pi = 1/2^+$ for ^{3}H and ^{3}He, and the resulting Hamiltonian matrices $\mathcal{H}_i$ are evaluated for the smallest eigenvalue on the QFP, as described in the Methods section.

The data of Table I depicted in Fig. 3 shows the ground-state energies of ^{3}H, ^{3}He, and ^{4}He computed with the VQE algorithm on the QFP as a function of the effective spatial extent, L, of the model space. For the weakly bound three-nucleon states of ^{3}H and ^{3}He, the energy is found to decrease noticeably with increasing L. For these systems as well as ^{4}He, extrapolations to large model spaces can be reliably performed (shown as shaded regions) using the leading-order expression given in Eq. (C2). For each nucleus, the model-space-extrapolated binding energy (shown as the red point at right) is consistent within systematic-dominated uncertainties with the corresponding tuned NLO EFT prediction. We note that the underlying Hamiltonian of NLO pionless EFT is known to reproduce experimental data to much better than the

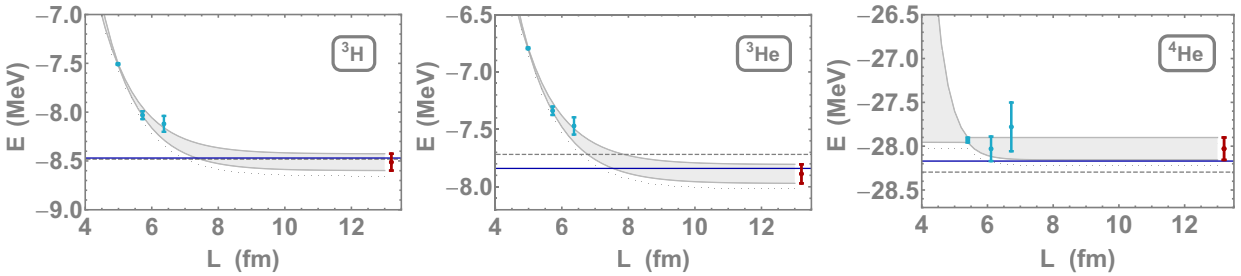

FIG. 3. Results of the nuclear ground-state energies for ^{3}H, ^{3}He, and ^{4}He nuclei computed with the QFP (blue data points) for Hilbert spaces with effective spatial extent L with estimated systematic uncertainties. Also shown are the leading-order extrapolations [see Eq. (C2)] to infinite model spaces with propagated uncertainties (gray bands), the resulting extrapolated energies E_∞ (red point at right), the tuned NLO EFT predictions (dark blue solid line), and the known high-precision values of the binding energies (dashed gray line).

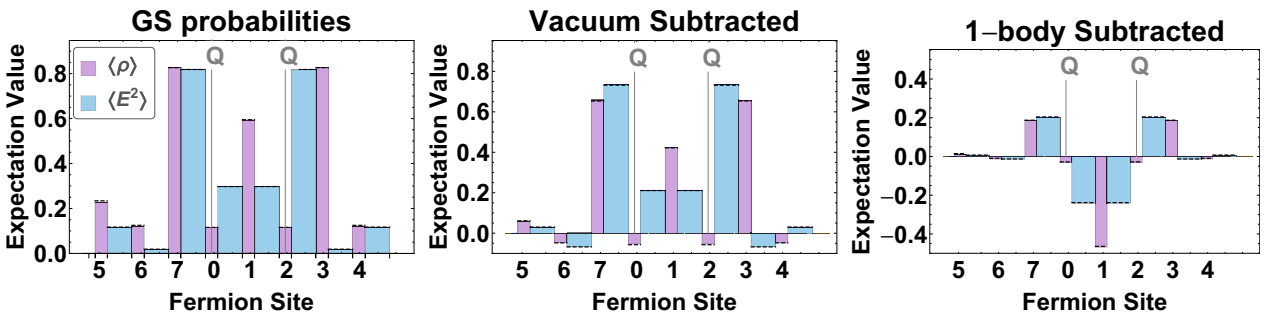

FIG. 4. The e^+e^- densities ($\langle\rho\rangle$) and energy density in the electric field ($\langle E^2\rangle$) for $Q=-1$ static charges separated by one spatial lattice site. The left panel shows the raw distributions, the center panel has the vacuum removed, and the right panel also has the contributions from the individual charges removed. The horizontal black dashed lines are the analytic values of the local densities, while the error bands (not seen on this scale) represent fluctuations over the last ten iterations of the VQE. The values shown in each panel are presented in Table VI in Appendix F.

naive ∼10% accuracy based upon power counting due to the relative size of coefficients in the effective range expansion.

V. SCHWINGER-MODEL SIMULATIONS

Quantum electrodynamics in 1+1 dimension, the Schwinger model [65,66], has been long studied as an example of confinement and chiral symmetry breaking in quantum field theory [67] and is receiving new attention in the context of quantum simulation [21,23,68–75]. To represent this continuous theory on computational devices, we employ staggered fermions [76] mapped to spin degrees of freedom as shown in Eq. (D1). Fluctuations in the truncated, quantized electric field are accompanied by pair (e^+e^-) creation and annihilation satisfying Gauss's law. Previous works have calculated static and dynamic observables resulting from these fluctuations on quantum devices [21,23]. In this article, we introduce nondynamical static charges, which are screened by deformations in the quantum vacuum and interact with the fermions only through their contribution to Gauss's law. Such systems are analogous to mesons found in nature containing a bottom or charm quark; thus we denote them "heavy mesons." The Hilbert space of each static-charge distribution is reduced by enforcing Gauss's law and projecting onto ground-state quantum numbers of parity and charge conjugation.

The energy and wave function of the vacuum, of single static charges, of two like-sign and two opposite-sign static charges separated by a distance r, and of three static charges of the distinct charge combinations separated by distances r_{12} and r_{13} were calculated on the QFP by applying VQE to eight-fermion-site, Schwinger-model Hamiltonians. These solutions may be combined to compute the heavy-meson mass, the full potential energy between two and three static

TABLE I. Simulation results for the ground-state energies of the light nuclei at NLO in the pionless EFT obtained with the QFP. The first two columns designate the nucleus (model space) and the dimensionality of the Hilbert space. The third column indicates the computations per iteration. The energy and associated standard deviation are quoted from the last five iterations of a converged VQE (statistical uncertainty only). The final column indicates the total time to complete 25 iterations.

	d	Computations/ Iteration	VQE energy	Time (min)
^{3}H ($N_{\max}=2$)	5	10	−7.5075(1)	2.3
^{3}H ($N_{\max}=4$)	15	105	−8.031(6)	27.1
^{3}H ($N_{\max}=6$)	34	561	−8.12(2)	134.6
^{3}He ($N_{\max}=2$)	5	10	−6.7942(1)	2.3
^{3}He ($N_{\max}=4$)	15	105	−7.3380(3)	26.9
^{3}He ($N_{\max}=6$)	34	561	−7.470(9)	133.8
^{4}He ($N_{\max}=2$)	5	10	−27.9301(2)	2.2
^{4}He ($N_{\max}=4$)	20	190	−28.03(1)	48.6
^{4}He ($N_{\max}=6$)	64	2016	−27.78(2)	500

TABLE II. Simulation results for ground-state energies in the Schwinger model obtained using the QFP. The first two columns designate the configuration of static charges and the symmetry-projected dimensionality of the Hilbert spaces. The third column indicates the computations per iteration [less than $d_{\rm sym}(d_{\rm sym}-1)/2$ due to matrix sparsity]. The energy and associated standard deviation are quoted from the last ten iterations of a converged VQE. The final column indicates the total time to complete 50 iterations.

	$d_{\rm sym}$	Computations/ Iterations	VQE energy	Time (min)
Vac	9	15	−2.01503(1)	7.1
(0)	26	154	−0.73167(2)	75
(0,0)	9	21	0.91843(2)	11.4
(0,2)	16	42	0.68691(1)	20.1
(0,4)[a]	17	45	0.59856(6)	67.0
(0,1)	41	225	−0.92433(2)	99.3
(0,3)[b]	58	222	0.289190(9)	298
(0,0,0)	7	15	6.42752(8)	7.3
(0,0,2)	5	9	2.428332(1)	4.5
(0,0,4)	5	9	2.300160(2)	4.7
(0,2,4)	5	9	2.210773(3)	4.7
(0,0,1)	59	385	0.5418(4)	173
(0,0,3)	31	87	1.83890(1)	40.1
(0,2,1)	35	217	0.22861(4)	99.6
(0,2,3)	62	406	0.3731(1)	194.6
(0,2,5)	24	105	1.535129(9)	46.9
(0,4,1)	68	448	0.3466(3)	196.8

[a]Obtained with three beamsplitters and 100 iterations.
[b]Obtained with 150 iterations.

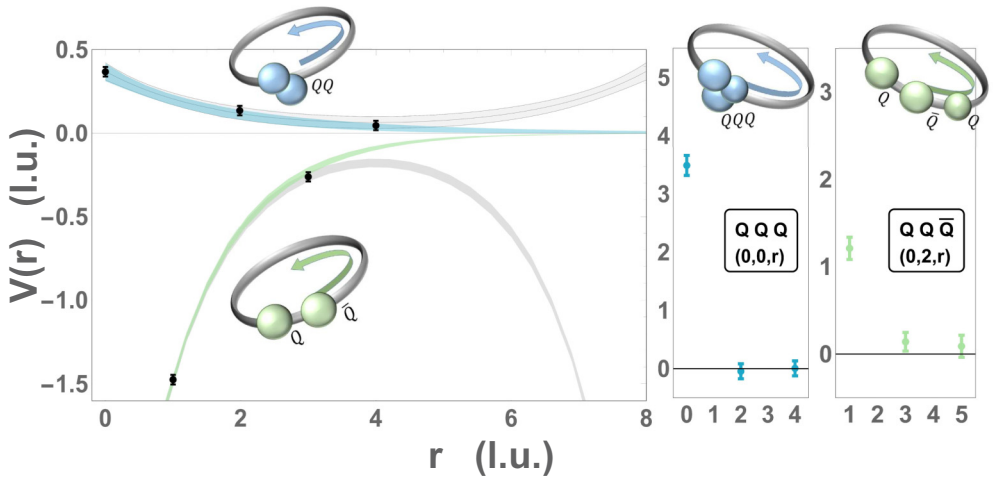

FIG. 5. The left panel shows the potential between two like-sign static-charged sources (upper curves) and between opposite-sign charges (lower curves) as a function of separation (in lattice units). The symmetric gray curves represent the extracted lattice potential, including the presence of image charges. The blue and green bands represent the infinite-volume potentials using correlated extracted values of the couplings and masses (see Appendix E for details). The center panel shows the three-body potential for three like-sign static charges. The right panel shows the three-body potential for two like-sign and one opposite-sign static charges.

charges over a range of separations, and local modifications to the vacuum structure due to static charges. As an example, Fig. 4 shows the local e^+ and e^- probabilities and energy density of the electric field for the ground state of two static negative charges with separation ($r = 2$), computed from the VQE results (see Table II). Using this and the other four configurations of two-body static charges (see Appendix A and E), Fig. 5 (left) shows the potential energy as a function of separation. For distances large compared with the radius of the heavy meson, the potential is expected to fall as the sum of exponentials with arguments set by the light-hadron spectrum. Short-distance deviations from these forms are expected to be a small effect in subsequent analyses. Fitting to the results of the QFP, including the effect of image charges from the boundary conditions, and isolating the infinite-volume limit, gives the phenomenological fit potentials in Fig. 5. These phenomenological potentials are matched through the Schrödinger equation to a low-energy EFT description of the Schwinger model in terms of local contact operators, the analog of the pionless theory, $\mathcal{H} = -C_N(N^\dagger N)^2 + \cdots$ at leading order for a given heavy-meson mass. The three-body potentials are extracted in similar ways, with the two-body potentials removed. Two slices of the three-body potential are displayed in Fig. 5 (right two panels), showing expected rapid suppression as the bodies separate. Phenomenological three-body potentials can further be extracted and used to constrain the coefficients of three-body EFT parameters.

Note that the demonstrated calculation is for a single lattice spacing and spatial volume. Modifying these parameters towards the continuum would provide higher resolution of extracted potentials and corresponding EFT parameters.

VI. DISCUSSION

Establishing a direct connection between the fundamental building blocks of our universe, the quarks and gluons, and the properties and dynamics of matter under a range of conditions faces challenges beyond the capabilities of foreseeable classical computation. From exponentially-growing Hilbert spaces required to describe nuclei, to sign problems in evaluating finite density systems, anticipated developments in quantum devices and quantum information offer the hope of addressing Grand Challenge problems in subatomic physics. For example, VQE algorithms implemented with error-corrected qubits are anticipated to provide a scalable path to solving these problems on future quantum devices. However, currently available hardware is too noisy to demonstrate such quantum advantages. Here we explored a way to implement VQE optically using the QFP with classical preprocessing. In particular, we use classical resources to project many-body fermionic Hamiltonians corresponding to nuclear and quantum field theory systems onto a hierarchy of single-particle Hamiltonians that can be simulated efficiently on the QFP. This demonstration of controlled, single-photon-equivalent, quantum-correlated manipulation is a first step towards scalable QFP simulations where input states are modified to consist of multiple photons. Together, the QFP and such state preparation of higher complexity is expected to require resources that scale polynomially with the size of the quantum system and thus exhibit a quantum advantage.

In this work, we have presented results from the largest photonics-based quantum simulation, using an all-optical quantum frequency processor, to demonstrate the potential of quantum technology for calculations in subatomic physics. We presented the two- and three-body interactions between composite objects informing the low-energy EFT of the Schwinger model, which shares characteristics with QCD. Further, representing a key ingredient in the connection between quarks, gluons, and nuclei, a low-energy EFT of QCD was used to calculate the binding energies of ^{3}H, ^{3}He, and ^{4}He. While the results of our calculations are not of comparable complexity or precision to those that can be achieved today with classical computation, they are an

encouraging first step in exploring the utility of optical quantum devices for addressing "Grand Challenges" in subatomic physics.

The U.S. Department of Energy (DOE) will provide public access to these results of federally sponsored research in accordance with the DOE Public Access Plan [93].

ACKNOWLEDGMENTS

N.K. and M.J.S. would like to thank Silas Beane, David Kaplan, and Aidan Murran for valuable discussions. This material is based upon work supported by the U.S. Department of Energy, Office of Science, Office of Nuclear Physics under Awards No. DEFG02-96ER40963 (University of Tennessee) and No. DE-SC0018223 (SciDAC-4 NUCLEI). N.K. and M.J.S. were supported by DOE Grant No. DE-FG02-00ER41132. N.K. was supported in part by the Seattle Chapter of the Achievement Rewards for College Scientists (ARCS) Foundation. A.E. received funding from the European Research Council (ERC) under the European Union's Horizon 2020 Research and Innovation Program (Grant Agreement No. 758027). This work is partially supported by the U.S. Department of Energy, Office of Science, Office of Advanced Scientific Computing Research (ASCR) quantum algorithm teams and testbed programs, under Field Work Proposals No. ERKJ333 and No. ERKJ335. Oak Ridge National Laboratory is managed by UT-Battelle, LLC, under Contract No. DE-AC05-000R22725 for the U.S. Department of Energy. The U.S. Government retains, and the publisher, by accepting the article for publication, acknowledges that the U.S. Government retains a nonexclusive, paid-up, irrevocable, worldwide license to publish or reproduce the published form of this manuscript, or allow others to do so, for U.S. government purposes. H.-H.L. and A.M.W. were supported in part by NSF Grant No. 1839191-ECCS.

APPENDIX A: RESULTS

The following section provides details of the VQE implementation on the QFP for the light nuclei and Schwinger-model systems presented in the main text.

APPENDIX B: OPTIMIZATION

In order to optimize the parameters of the trial wave functions employed in this work, we have implemented an approximate gradient method based on the measured reduced density matrix elements. For calculating the derivative of the energy employing the UCC wave function of Eq. (2), a single gradient element becomes

$$\chi_k = \frac{\delta\langle\mathcal{H}_{\rm SQ}\rangle}{\delta\Theta_k} = \langle\Psi|[c_0^\dagger c_k, \mathcal{H}_{\rm SQ}]|\Psi\rangle + \text{H.c.}$$
$$= 2\sum_l (\rho_{0l}h_{lk} - \rho_{kl}h_{l0})\,, \tag{B1}$$

where it should be noted that this expression depends only on the already-measured reduced density matrix elements used to evaluate the energy. Once scaled by an appropriate quantity Δ, which is analogous to a time step, each parameter can be updated as follows:

$$\Theta_k \to \Theta_k + \Delta\chi_k\,. \tag{B2}$$

This procedure was iterated until a change in energy dropped below a given threshhold.

For systems where the initial trial wave function for the ground state was nondegenerate, an additional step was taken to improve convergence. The elements of Eq. (B1) vary quite radically, both in their absolute size and the rate at which they vanish as the minimum is approached. Drawing from the similarity of this method to [57,77], it is clear that one can do appreciably better by normalizing the elements to the diagonal Hamiltonian matrix elements, yielding a new update procedure:

$$\Theta_k \to \Theta_k + \Delta\frac{\chi_k}{h_{kk} - h_{00}}\,. \tag{B3}$$

For the systems treated in this work, this modification decreased the number of steps required to reach convergence by a factor of 2–3.

APPENDIX C: NUCLEAR STRUCTURE

A Hamiltonian from the NLO pionless EFT [38,60–62], a systematically improvable approach to nuclear interactions at low energies, is employed for computations of the nuclei ^{3}H, ^{3}He, and ^{4}He, with a momentum-space potential

$$V = V_{NN}^{(^1S_0)}(p', p) + V_{NN}^{(^3S_1)}(p', p) + V_{NNN}\,,$$
$$V_{NN}^{(^1S_0)}(p', p) = \tilde{C}_{^1S_0} + C_{^1S_0}(p'^2 + p^2)\,,$$
$$V_{NN}^{(^3S_1)}(p', p) = \tilde{C}_{^3S_1} + C_{^3S_1}(p'^2 + p^2)\,,$$
$$V_{NNN} = \frac{c_E}{F_\pi^4\Lambda_\chi}\sum_{1\leqslant i\neq j\leqslant A}\vec{\tau}_i\cdot\vec{\tau}_j\,. \tag{C1}$$

Here, p and p' denote magnitudes of the incoming and outgoing relative three-momentum, respectively. The nucleon-nucleon potentials V_{NN} act in the singlet and triplet S waves, with $\tilde{C}_{^1S_0} = -0.7617$ MeV^{-2}, $C_{^1S_0} = 2.9098$ MeV^{-4}, $\tilde{C}_{^3S_1} = -1.2014$ MeV^{-2}, and $C_{^3S_1} = 3.3984$ MeV^{-4}, respectively. These parameters were determined by fits to the effective range expansion in the respective partial waves and to the deuteron binding energy. The three-nucleon potential V_{NNN} employs the isospin operators $\vec{\tau}_i$ for the nucleon i, the parameters $F_\pi = 92.4$ MeV, and $\Lambda_\chi = 700$ MeV. The parameter $c_E = 0.019\,29$ is adjusted to reproduce the triton binding energy. This EFT is implemented as a discrete variable representation (DVR) [78–80] in the harmonic oscillator basis, using translationally invariant Jacobi coordinates and the infrared corrections of Refs. [36,81]. The potentials act only between states with excitation energies up to and including $2\hbar\omega$, while the kinetic energy is not truncated. While our results are insensitive to the ultraviolet cutoff of the potential, we have chosen to work with a cutoff of 337 MeV and $\hbar\omega = 22$ MeV. Figure 6 shows phase shifts in the singlet and triplet S-wave channels obtained from the pionless theory with matched EFT parameters and compares them to the corresponding phase shifts obtained from the high-precision CD Bonn potential [82]. Our NLO EFT potentials reproduce the phase shifts within uncertainty estimates. These systematic theory uncertainties, shown as shaded regions in Fig. 6, result from estimates of the

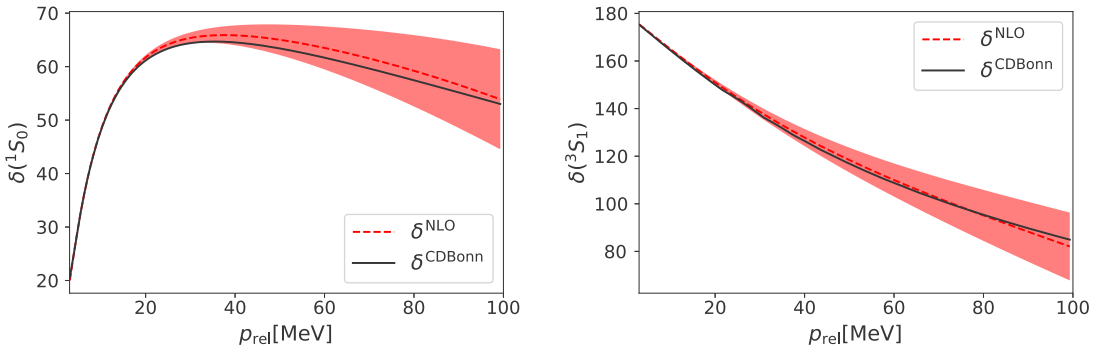

FIG. 6. Nucleon-nucleon phase shifts in the singlet (left) and triplet (right) S-wave channels (in degrees) as a function of relative momentum. The solid (black) lines correspond to high-precision results obtained with the CD Bonn potential. The dashed (red) lines correspond to results obtained from the NLO pionless EFT, while the shaded (red) region includes estimates from higher orders in the pionless EFT expansion that are not included in the interactions employed on the QFP.

contributions from terms that are higher order (NNLO) in the pionless EFT but are not included in our calculations.

Using standard tools [83,84], Hamiltonian matrices in Hilbert spaces with spin and parity $J^\pi = 1/2^+$ and 0^+ for the three-nucleon systems ^{3}H, ^{3}He, and ^{4}He, respectively, are computed. Limiting the total number of harmonic oscillator quanta to $N_{\rm max} = 2, 4, 6$ leads to dense Hamiltonian matrices of dimension $d = 5, 15, 34$ and $d = 5, 20, 64$ for the nuclei with mass numbers $A = 3$ and $A = 4$, respectively. These Hamiltonian matrices provide the inputs for the VQE algorithm.

At low energies, states projected onto a finite harmonic oscillator basis closely resemble those projected onto modes of a spherical cavity with a hard-wall radius $L \sim [N_{\rm max}/(m\omega)]^{1/2}$ [85]. It can be shown [85], using a development that parallels that of Lüscher and others, that to establish finite-volume corrections to localized states in lattice QCD calculations [86,87], the leading finite-model-space shifts in the energy of an isolated bound state have the form

$$E(L) = E_\infty + ae^{-2k_\infty L}. \tag{C2}$$

From bound-state energies $E(L)$ determined in three finite model spaces, and the separation momentum

$$k_\infty = \frac{1}{\hbar}\sqrt{-2m[E_\infty(A) - E_\infty(A-1)]} \tag{C3}$$

of the A-body system [88,89], we determine the amplitude a and the infinite-model-space energy E_∞ by a fit. Using the values of L tabulated in the Supplemental Material of Ref. [90], the binding energies $E(L)$ computed in finite model spaces using our QFP, that are shown in Table III, are extrapolated to infinite model spaces.

Table III also shows the results of exact diagonalizations of the Hamiltonian matrices describing the light nuclei in Hilbert spaces with a range of $N_{\rm max}$, as indicated. Diagonalizations in large model spaces of size N_A ($N_3 = 40$ and $N_4 = 20$ for nuclei with mass number $A = 3$ and $A = 4$, respectively) are essentially converged with respect to the size of the model space. The infinite-model-space extrapolation results obtained by fitting Eq. (C2) to the data obtained with $N_{\rm max} = 2, 4, 6$ are also shown; these results are close to the (essentially) exact numerical results, and higher-order corrections to the leading-order result (C2) are suppressed by powers and exponentials of $k_\infty L$ [91]. Our extrapolated results for ^{3}He and ^{4}He are close to their experimental values, consistent with expectations from a leading-order Hamiltonian within statistical and systematic uncertainties. (We remind the reader that the three-body EFT parameter was adjusted to reproduce the ground-state energy of ^{3}H.) The results obtained from the QFP, that are shown in Fig. 3 of the main text, are also given in Table III. Through repeated measurements using the

TABLE III. Ground-state energies of light nuclei obtained from Hamiltonian diagonalization of the NLO pionless EFT using the QFP compared to the exact results for model spaces of size $N_{\rm max} = 2, 4, 6$ and their extrapolation to infinite model space $N_{\rm max} = \infty$. For comparison, the experimentally known values are given (Exp.), along with the results obtained from exact diagonalizations in a large model space, N_A. For the quantum frequency processor, systematic simulation uncertainties of (0.1%, 0.5%, 1%) in the VQE for $N_{\rm max}$ of (2, 4, 6) are extrapolated to the infinite model space as shown in Fig. 3 of the main text. This extrapolation uses the form of Eq. (C2), defining k_∞ through the separation energy and enforcing the constraint $a < 1$ GeV.

	Quantum frequency processor			Exact diagonalization		
$N_{\rm max}$	^{3}H	^{3}He	^{4}He	^{3}H	^{3}He	^{4}He
2	−7.508(8)	−6.794(7)	−27.93(3)	−7.513	−6.800	−27.947
4	−8.031(40)	−7.338(37)	−28.03(14)	−8.060	−7.366	−28.106
6	−8.120(81)	−7.470(75)	−27.78(28)	−8.275	−7.600	−28.148
N_A	—	—	—	−8.482	−7.830	−28.165
∞	−8.51(9)	−7.89(8)	−28.04(14)	−8.47	−7.84	−28.17
Exp.	−8.482	−7.718	−28.296	−8.482	−7.718	−28.296

QFP, we have identified a systematic uncertainty of ±1% that accompanies each measurement, which is significantly larger than the associated statistical uncertainties. In extrapolating to infinite model space, this systematic uncertainty of each point is uniformly sampled over in performing a Monte Carlo to determine the uncertainty of each binding energy as a function of L, including the $L \to \infty$ limit. For each nucleus, a value of the binding for each of the three measured L values is uniformly sampled from the interval arising from the systematic uncertainty. These samples are then used in a two-parameter fit of the form in Eq. (C2), where the difference in binding energies is used to relate k_∞ to E_∞ via Eq. (C3). These fit parameters define a curve as a function of L. This process is repeated a large number of times to establish the shaded fit region and infinite-model-space value.

APPENDIX D: LATTICE HAMILTONIANS FOR SCHWINGER-MODEL SIMULATIONS

In 1 + 1 dimensional quantum electrodynamics, latticized with staggered fermions [76] and transformed to spin degrees of freedom using the Jordan-Wigner transformation, the Hamiltonian of the Schwinger model [65,66] can be written as

$$\tilde{\mathcal{H}}_{\mathrm{SQ}} = x \sum_{n=0}^{N_{fs}-1} (\sigma_n^+ L_n^- \sigma_{n+1}^- + \sigma_{n+1}^+ L_n^+ \sigma_n^-) + \sum_{n=0}^{N_{fs}-1} \left(\ell_n^2 + \frac{\mu}{2}(-)^n \sigma_n^z \right). \tag{D1}$$

The kinetic (hopping) term contains raising and lowering operators $L^\pm$, modifying the value of the electric field that is naturally quantized (between truncations $\pm\Lambda$) in one dimension. Choosing periodic boundary conditions for this one-dimensional spatial lattice produces a Hamiltonian with discrete rotational symmetry. While this representation is perfectly suited for qubit implementation—creating a latticized, tensor-product structure with single qubits at the sites to represent fermion occupation and registers of $\lceil \log_2(2\Lambda + 1) \rceil$ qubits on each link for the electric field—the additional constraint of Gauss's law makes this representation both excessive for physical states and sensitive to noise within the quantum computation. Instead, the lattice configurations in the physical sector (that satisfy Gauss's law) are classically enumerated and mapped onto quantum states of the Hamiltonian. Because of the locality of interactions, the Hamiltonian remains sparse in this representation. By working only with configurations in the physical subspace, the Hilbert space dimension in terms of N_s, the number of spatial sites, is reduced from $e^{\log(64)N_s}$ to $1.02(1)e^{1.1772(2)N_s}$ and the four-spatial-site lattice becomes accessible to our QFP.

In order to calculate the mass of the heavy meson M_H, comprised of a static charge (denoted by Q or $\bar{Q}$) and light degrees of freedom, as well as the two- and three-body potentials, 17 different configurations of up to three static charges are needed on a four-spatial-site lattice: the empty configuration of the vacuum, a single static charge, five separations of two static charges, and ten three-static-charge configurations. These configurations are detailed in Table IV. In the second column of this table, the symmetric gauge field truncation

TABLE IV. Properties of the systems studied with our quantum device. The first column indicates the locations of static charges [with charge $-Q$ ($+Q$) for odd (even) sites, respectively]. The electric field truncation Λ determines the dimension of the underlying Hilbert space d, and symmetries of the static-charge configuration allow reductions to d_{sym}. The values of Λ are chosen to achieve sub-% precision in the ground-state energy and representative wave functions.

	Λ	d	Symmetries	d_{sym}	E_{GS} precision
Vac	3	53	P, $\vec{p}$	9	0.2%
(0)	4	50	P	26	0.4%
(0,0)	5	16	P	9	0.2%
(0,2)	5	31	P	16	0.09%
(0,4)	5	35	P	17	0.05%
(0,1)	5	67	CP	41	0.8%
(0,3)	8	95	CP	58	0.15%
(0,0,0)	12	13	P	7	5×10^{-7}%
(0,0,2)	5	5		5	0.04%
(0,0,4)	4	5		5	0.6%
(0,2,4)	4	9	P	5	0.1%
(0,0,1)	7	59		59	0.13%
(0,0,3)	7	31		31	0.7%
(0,2,1)	6	67	P	35	0.6%
(0,2,3)	7	62		62	0.1%
(0,2,5)	7	46	P	24	0.74%
(0,4,1)	7	68		68	0.1%

Λ is chosen to reduce truncation systematic errors on the ground-state energy to below the 1% precision, expected to be attainable with optical quantum hardware.

While the systems studied can be numerically solved with high precision using classical techniques, their dimensionalities are nontrivial with respect to the capabilities of present-day quantum computing devices. With this in mind, it is convenient to further reduce the latticized, electric-field-truncated Hamiltonians by projecting into the symmetry sectors of momentum $\vec{p}$, parity (P), and charge parity (CP), as done in Ref. [21]. For all but the vacuum state, the presence of static charges at specified lattice points removes the possibility of momentum projecting—the discrete, rotational symmetry of the lattice has been broken. Beginning with a Hilbert space dimension of 53, projecting the vacuum to the zero-momentum subspace by creating a basis of rotationally invariant linear combinations results in a vastly reduced Hilbert space of dimension 15—a size amenable with only four qubits. Further projecting the vacuum into a sector of positive parity about any one of the four rotationally equivalent symmetry axes results in a nine-dimensional Hilbert space to be explored with optical hardware. Such parity projections are possible for eight of the static charge configurations about unique parity axes (e.g., parity axis through sites 2 and 6 for static charges located at 0, 2, 4).

Configurations containing one Q and one $\bar{Q}$ do not contain states of definite parity but, rather, of parity and charge conjugation. As illustrated in Ref. [21], charge conjugation on a staggered lattice of fermions may be consistently defined by altering the sign of all charges and introducing a shift of a half-spatial site in order to maintain the staggered distribution

of the two-component Dirac spinor with negative (positive) charges on even (odd) fermion sites. For example, in the case of Q and $\bar{Q}$ at locations 0 and 3, respectively, a parity axis between fermion sites 1 and 5 and a subsequent charge conjugation with clockwise half-spatial-site shift defines a valid CP symmetry:

$$C_+P|Q\cdot\cdot\bar{Q}\cdot\cdot\cdot\cdot\rangle = C_+|\cdot\cdot Q\cdot\cdot\cdot\bar{Q}\rangle = |Q\cdot\cdot\bar{Q}\cdot\cdot\cdot\cdot\rangle. \quad \text{(D2)}$$

Projecting into a sector of positive CP, the sector containing the ground state of the Q and $\bar{Q}$ system results in a Hilbert space dimensionality reduction from 95 to 58 states. This brings the system within reach of advances in quantum optical devices presented in the main text.

APPENDIX E: POTENTIALS AND EFFECTIVE INTERACTIONS FROM SIMULATIONS OF THE SCHWINGER MODEL

Hybrid classical-quantum VQE calculations were performed to determine ground-state energies of systems containing two or three static charges from a set of Hamiltonian matrices, providing both eigenvalues and eigenvectors through a customized VQE algorithm using the UCC ansatz. Differences between these ground-state energies and their wave functions reveal the interaction potentials between the static charges and the induced modifications to the vacuum charge distributions. To compute the potential energy between static charges located at $r = 0$ and $r = 3$, for example, the ground-state energy of the Hamiltonian matrix defining the truncated Hilbert space with one charge located at $r = 0$ and an anticharge located at $r = 3$, $E^{(Q\overline{Q})}(0, 3)$, is determined along with the wave function. From these the energy of the vacuum is removed to give $\Delta E^{(Q\overline{Q})}(3) = E^{(Q\overline{Q})}(0, 3) - E^{\text{vac}}$. This energy difference is independent of where it is evaluated by the discrete rotational symmetry and CP symmetry of the lattice discretization. A similar calculation is performed of the energy of a single static charge, $E^{(Q)}(0)$, that leads to the mass of the heavy meson, $M_H = E^{(Q)}(0) - E^{\text{vac}}$. The two-body potential between the static charges is defined by the difference $V^{(Q\overline{Q})}(3) = \Delta E^{(Q\overline{Q})}(3) - 2M_H$. The other two-body potentials, $V^{(QQ)}(r)$ and $V^{(Q\overline{Q})}(r)$ for r even and odd respectively, are found similarly. Extraction of the three-body potentials requires a further subtraction, and as an example, consider the potential between static charges at $r = 0$ and $r = 2$ and a static anticharge at $r = 3$. The energy of the vacuum is subtracted from the ground-state energy, $\Delta E^{(QQ\overline{Q})}(0, 2, 3) = E^{(QQ\overline{Q})}(0, 2, 3) - E^{\text{vac}}$. From this, the masses of three heavy mesons are removed, $\Delta^2 E^{(QQ\overline{Q})}(0, 2, 3) = \Delta E^{(QQ\overline{Q})}(0, 2, 3) - 3M_H$. To define the residual three-body potential, the contributions from the two-body interactions are removed, $V^{(QQ\overline{Q})}(0, 2, 3) = \Delta^2 E^{(QQ\overline{Q})}(0, 2, 3) - V^{(QQ)}(2) - V^{(Q\overline{Q})}(1) - V^{(Q\overline{Q})}(3)$. The values obtained in the simulation for the vacuum energy, the mass of the heavy meson, the two- and three-body potentials, obtained with a mass $\mu = 0.1$ and hopping term coefficient $x = 0.6$ defining the Schwinger-model Hamiltonian, are given in Table V. The two- and three-body potentials are displayed in Fig. 5 of the main text and Fig. 8 appearing later in this section.

TABLE V. The vacuum energy, the mass of the heavy meson, and the two- and three-body potentials extracted from the VQE implementation. The uncertainties result from propagating 1% systematic uncertainties in the simulated ground-state energies. The second column indicates the Jacobi coordinates for the three-body systems. The final column shows the calculated values of the potentials at the simulation-implemented values of Λ, electric field truncation.

$\mathcal{O}$	(R_1, R_2)	$\langle\mathcal{O}\rangle \pm \sigma_{\mathcal{O}}$	Exact
E_{vac}		-2.014 ± 0.020	-2.0158
M_H		1.283 ± 0.021	1.2825
$V^{QQ}(0)$		0.368 ± 0.048	0.3683
$V^{QQ}(2)$		0.136 ± 0.048	0.1372
$V^{QQ}(4)$		0.047 ± 0.048	0.0482
$V^{Q\bar{Q}}(1)$		-1.475 ± 0.048	-1.4756
$V^{Q\bar{Q}}(3)$		-0.262 ± 0.047	-0.2606
$V^{QQQ}(0, 0, 0)$	(0, 0)	3.49 ± 0.17	3.4901
$V^{QQQ}(0, 0, 2)$	(0, 2)	-0.05 ± 0.13	-0.0464
$V^{QQQ}(0, 0, 4)$	(0, 4)	0.00 ± 0.13	0.0033
$V^{QQQ}(0, 2, 4)$	(2, 3)	0.06 ± 0.13	0.0561
$V^{QQ\bar{Q}}(0, 0, 1)$	(0, 1)	1.29 ± 0.13	1.2872
$V^{QQ\bar{Q}}(0, 0, 3)$	(0, 3)	0.16 ± 0.13	0.1591
$V^{QQ\bar{Q}}(0, 2, 1)$	(2, 0)	1.21 ± 0.13	1.2097
$V^{QQ\bar{Q}}(0, 2, 3)$	(2, 2)	0.14 ± 0.11	0.1383
$V^{QQ\bar{Q}}(0, 2, 5)$	(2, 4)	0.09 ± 0.13	0.0867
$V^{QQ\bar{Q}}(0, 4, 1)$	(4, 1)	0.20 ± 0.11	0.2008

The ground-state energies determined with VQE have both statistical uncertainties, determined by variations in the last several iterations, and systematic uncertainties. The dominant systematic uncertainty is reproducibility of the simulation results, which was estimated by variations in results collected during multiple long runs on a representative set of Hamiltonian matrices, repeated throughout the course of the data collection. This variation was found to be less than 1%, and we assign a systematic uncertainty of 1% to each energy measurement as a conservative estimate.

Beyond numerical determination of the two-body potentials between static charges, it is worth making the connection to nuclear physics phenomenology through parametrization of the potentials based upon the spectrum of the Schwinger model, and through matching to the appropriate low-energy EFT. In the $1 + 1$ dimensional Schwinger model, the potential between charges falls with distance as the sum of exponentials, as the spectrum does not contain a massless particle. With the parameters that were used in the simulation, the number of measurements of the potentials are few: three for the QQ systems and two for the $Q\overline{Q}$ system. Consequently, we fit a single exponential in both channels, with the understanding that they are expected to reproduce the correct behaviors at long distances, but are merely parametrizations at intermediate and short distances. Results obtained for, and from, these parametrizations have associated unquantified model uncertainties. We write the parametrizations of the infinite-volume two-body potentials as

$$V^{(QQ)}(r) = \left(g^{(QQ)}\right)^2 e^{-M^{(QQ)}r},$$
$$V^{(Q\overline{Q})}(r) = -\left(g^{(Q\overline{Q})}\right)^2 e^{-M^{(Q\overline{Q})}r}, \quad \text{(E1)}$$

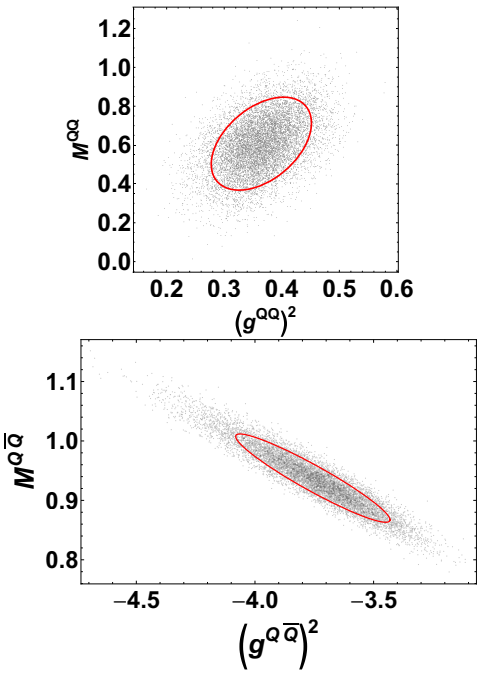

FIG. 7. Monte Carlo samples and 68% confidence ellipses of the couplings and masses of the QQ and $Q\overline{Q}$ two-body interactions. The ellipse associated with the QQ system (left panel) is described by eigenvectors $(0.176, 0.984)$ and $(-0.984, 0.176)$ with associated semiaxis radii 0.177 and 0.984. The ellipse associated with the $Q\overline{Q}$ system (right panel) is described by eigenvectors $(-0.977, 0.211)$ and $(-0.211, -0.977)$ with associated semiaxis radii 0.332 and 0.0236.

where the couplings, $g^{(QQ)}$ and $g^{(Q\overline{Q})}$, and the masses, $M^{(QQ)}$ and $M^{(Q\overline{Q})}$, are treated as fit parameters. We expect the masses to be close to the mass of the lightest vector meson but modified by the close proximity of other states.

As our calculations are performed in a finite volume subject to periodic boundary conditions, the potentials experienced by static charges are modified by the presence of image charges, separated by a distance nL, where n is an integer and L is the spatial extent of the lattice. As a result, the potentials extracted from our lattice calculations will be of the form [86,87]

$$V^{(j),L}(r) = \sum_{n=-\infty}^{+\infty} V^{(j)}(|r + nL|)\,, \tag{E2}$$

where $j = QQ, Q\overline{Q}$ correspond to the potentials in Eq. (E1). Fitting these forms for the two-body potentials to the results obtained with the QFP leads to

$$\begin{aligned} \left(g^{(QQ)}\right)^2 &= 0.365(52), \quad M^{(QQ)} = 0.61(14) \\ \left(g^{(Q\overline{Q})}\right)^2 &= 3.75(31), \quad M^{(Q\overline{Q})} = 0.937(71)\,, \end{aligned} \tag{E3}$$

where the quoted uncertainties are determined by projection of the elliptical contours of Fig. 7 onto each axis—the resulting uncertainties being slightly enlarged with respect to those quoted for single-variable, marginalized probability distributions. These quantities have support in the ultraviolet structure of the theory and are modified in the finite volume by

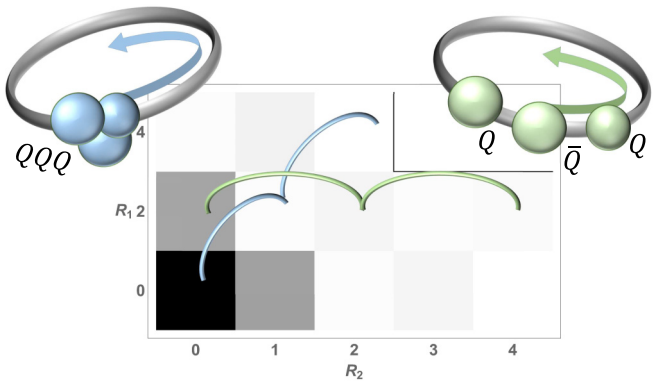

FIG. 8. The potential between three static charges represented by Jacobi coordinates in one dimension, $R_1 = |r_2 - r_1|$ and $R_2 = |r_3 - \frac{R_1}{2}|$, with $r_{1,2,3}$ the QQQ or $QQ\overline{Q}$ distances from the origin. The physical configurations of static charges on the lattice associated with the blue and green paths through the grid of three-body potential values are depicted by the schematic diagrams at the corners.

terms that are exponentially small, determined by the ratio of ΛL, where Λ is the ultraviolet scale [86,87]. Assuming that there is a scale separation between the masses in the finite-volume effects and the ultraviolet scale, the fit parameters in the potentials can be used to extrapolate to an infinite volume simply by inserting them into the potentials in Eq. (E1). Both the periodic- and infinite-volume potentials are shown in the left panel of Fig. 5 of the main text.

These potentials can be used directly for phenomenological applications (in $1+1$ dimensions) for processes involving heavy mesons of finite mass and momentum up to the ultraviolet scale of the theory. Results from these potentials are expected to exhibit deviations from actual predictions of the Schwinger model due to the limited form fit to the data. For low-energy processes, calculations can be reorganized and generally made simpler by matching to a low-energy EFT with consistent power counting that is explicitly constructed to faithfully reproduce the low-energy behavior of S-matrix elements. In nuclear physics, the low-energy behavior (below the t-channel cut in one-pion exchange) of few-nucleon systems is reproduced by the pionless EFT [60–62], consisting of contact operators of δ functions and (covariant-)derivatives, and gauge-invariant operators describing interactions with external probes [92].

As an example, we outline the matching between the Schwinger model and its low-energy EFT, in which there are only dynamical heavy mesons. Using the fit values of the EFT parameters and their associated uncertainties in the infinite-volume $Q\overline{Q}$ potential, we solve the Schrödinger equation to produce zero-energy wave functions. Far from the potential, the wave functions are straight lines and define the scattering lengths. These wave functions can be reproduced by a δ-function potential, with strength C_0 arising from an effective potential of the form $V_{\rm eff}(r) = C_0\delta(r)$. For a heavy meson of mass $M_H^{(\rm EFT)} = 4.5$ that is chosen for the sake of demonstration only, $C_0 = -0.117(30)$, which should be compared to the naive estimate from the Born term of $C_0 = -8.0(0.2)$. The potential also admits two bound states, a "shallow" one with $E \sim -0.59$ and a deep one with $E \sim -2.4$, which corresponds to a positroniumlike state.

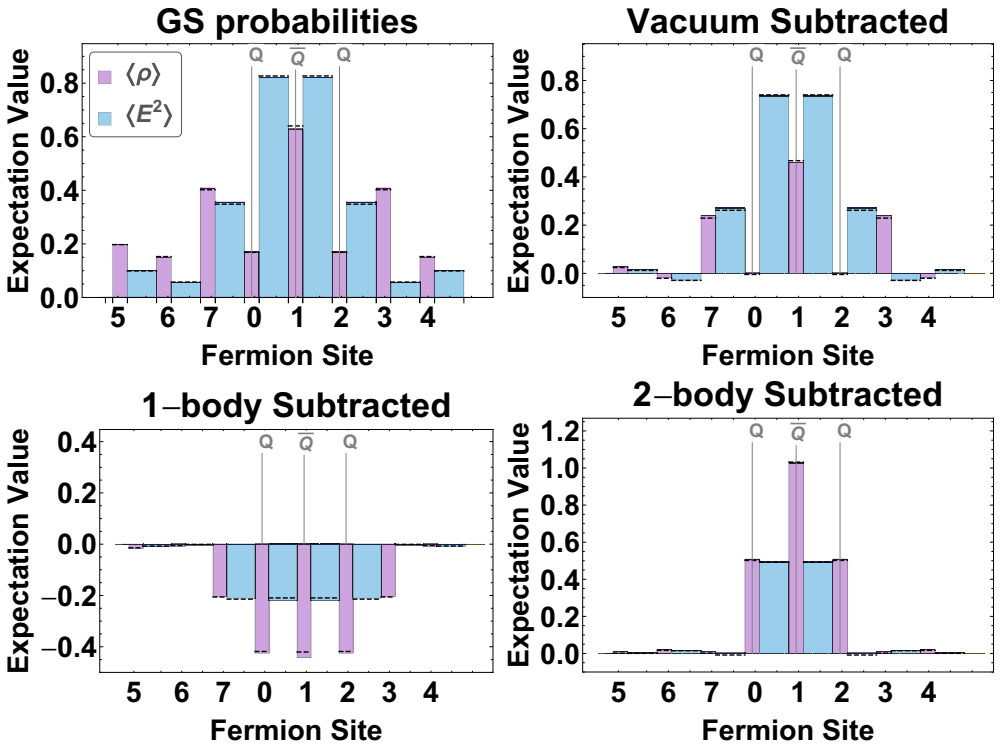

FIG. 9. Local properties of the vacuum with three static charges, with Q and $\bar{Q}$ located at lattice sites (0, 2) and 1, respectively. The uncertainties, which are too small to be visible, represent the stability of these local properties over wave functions extracted over the last ten VQE iterations. The horizontal dashed lines are the values calculated through exact diagonalization. The values shown in each panel are presented in Table VII.

It is convenient to work with Jacobi coordinates in presenting the three-body potentials. These relative coordinates are defined by $R_1 = |r_1 - r_2|$ and $R_2 = r_3 - R_1/2$, where we have worked with the convention that the first two particles are identified as those with the same charge. The results of our experiments are presented in Table V and displayed in Fig. 8. The three-body potentials are found to fall rapidly with either of the Jacobi coordinates, as expected. While these potentials could be matched to the low-energy EFT, with operator structures of the form $\mathcal{O} \sim (N^\dagger N)^3$, to be used in other more complex calculations, we leave that for future investigations.

The deformations to the vacuum structure resulting from these three-body forces, arrived at by taking differences in the energy density in the electric field and in the probabilities of the electron and positron states, have been calculated. In Fig. 9, we show the modifications to the vacuum structure for $V^{(Q\bar{Q}Q)}(0, 2, 1)$, corresponding to the three-body system with Jacobi coordinates $R_1 = 2$ and $R_2 = 1$.

A single-hadron quantity that we derive from our results is the charge radius of the heavy meson. Unlike classical lattice QCD calculations, where contributions from both connected-quark and disconnected-quark must be calculated, unless a

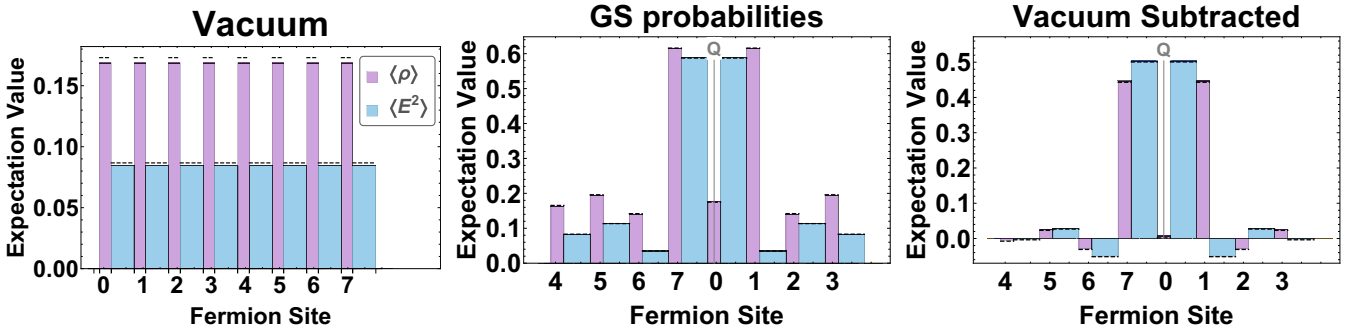

FIG. 10. Local properties of the vacuum and a single static charge located at $r = 0$ that creates a heavy meson. The uncertainties, which are too small to be visible, represent the stability of these local properties over wave functions extracted over the last ten VQE iterations. The horizontal dashed lines are the values calculated through exact diagonalization. The values shown in each panel are presented in Tables VIII and IX.

TABLE VI. Measured and exact expectation values for the local charge density and energy in the electric field as shown in Fig. 4 of the main text, with two static charges located at sites 0 and 2. The uncertainties on measured values represent statistical fluctuations over the last ten wave functions of the VQE iterations and do not include estimates of associated systematic uncertainties. Note, from Table IV, that parity has been enforced for this system, leading to spatially symmetric locations having the same values.

r	$\langle\rho\rangle$	$\langle\rho\rangle_{\text{exact}}$	$\langle E^2\rangle$	$\langle E^2\rangle_{\text{exact}}$
GS probabilities associated with two static charges at $r = 0, 2$				
0	0.115596(19)	0.115881	0.29668(15)	0.297446
1	0.59336(29)	0.594892	0.29668(15)	0.297446
2	0.115596(19)	0.115881	0.81892(16)	0.818435
3	0.82624(16)	0.826473	0.018040(24)	0.01883
4	0.121542(27)	0.125071	0.114283(24)	0.117114
5	0.228433(50)	0.234066	0.114283(35)	0.117114
6	0.121542(27)	0.125071	0.018040(25)	0.01883
7	0.82624(16)	0.826473	0.81892(16)	0.818435
Vacuum subtracted				
0	−0.053082(14)	−0.0571012	0.21208(15)	0.210749
1	0.42468(30)	0.42191	0.21208(15)	0.210749
2	−0.053082(14)	−0.0571012	0.73432(16)	0.731738
3	0.65757(15)	0.653491	−0.066560(31)	−0.0678671
4	−0.047135(27)	−0.0479109	0.029682(21)	0.0304174
5	0.059756(43)	0.0610843	0.029682(21)	0.0304174
6	−0.047135(27)	−0.0479109	−0.066560(31)	−0.0678671
7	0.65757(15)	0.653491	0.73432(16)	0.731738
1-Body subtracted				
0	−0.031897(61)	−0.0278071	−0.24139(13)	−0.238353
1	−0.46919(27)	−0.46415	−0.24139(13)	−0.238353
2	−0.031897(61)	−0.0278071	0.20279(19)	0.204377
3	0.18521(19)	0.187407	−0.0140797(97)	−0.012637
4	−0.013040(63)	−0.00937306	0.004098(51)	0.00738809
5	0.00891(10)	0.0149761	0.004098(51)	0.00738809
6	−0.013040(63)	−0.00937306	−0.0140797(97)	−0.012637
7	0.18521(19)	0.187407	0.20279(19)	0.204377

symmetry forbids one or both of the contributions, the quantum computation allows for a direct determination of relevant quantities from the wave function of the system. In the case of the heavy meson formed around a static quark at $r = 0$, the charge radius can be determined by a direct evaluation of the discrete sum

$$\langle r^2\rangle_Q = \sum_{n=0}^{N_Q/2} (-1)^n\, n^2\, \text{Prob}(n)\,, \tag{E4}$$

where $\text{Prob}(n)$ is the probability of finding an electron or positron at the nth site. The sum is cut off at half of the lattice to minimize the contribution from the image charges, introducing an uncertainty naively estimated to be the average size of the last two contributions. We find the square-charge radius of the heavy meson containing a positively charged static charge, determined from the charge distribution shown in Fig. 10, to be

$$\langle r^2\rangle_Q = -1.76(32) \tag{E5}$$

TABLE VII. Measured and exact expectation values for the local charge density and energy in the electric field as shown in Fig. 9, with three static charges located at sites $r = 0, 1, 2$. The uncertainties on measured values represent statistical fluctuations over the last ten wave functions of the VQE iterations and do not include estimates of associated systematic uncertainties. Note, from Table IV, that parity has been enforced for this system, leading to spatially symmetric locations having the same values.

r	$\langle\rho\rangle$	$\langle\rho\rangle_{\text{exact}}$	$\langle E^2\rangle$	$\langle E^2\rangle_{\text{exact}}$
GS probabilities associated with three static charges, at $r = 0, 1, 2$				
0	0.16927(16)	0.168397	0.82064(80)	0.826857
1	0.6272(17)	0.640306	0.82064(80)	0.826857
2	0.16927(16)	0.168397	0.35567(99)	0.348244
3	0.40786(86)	0.402136	0.05647(12)	0.057447
4	0.150959(62)	0.152525	0.099227(72)	0.0989282
5	0.19755(14)	0.197266	0.099227(72)	0.0989282
6	0.150959(62)	0.152525	0.05647(12)	0.057447
7	0.40786(86)	0.402136	0.35567(99)	0.348244
Vacuum subtracted				
0	0.00060(15)	−0.00458463	0.73604(81)	0.74016
1	0.4585(17)	0.467324	0.73604(81)	0.74016
2	0.00060(15)	−0.00458463	0.27107(99)	0.261547
3	0.23918(85)	0.229154	−0.02813(12)	−0.0292501
4	−0.017718(72)	−0.0204571	0.014626(67)	0.0122311
5	0.02887(14)	0.0242844	0.014626(67)	0.0122311
6	−0.017718(72)	−0.0204571	−0.02813(12)	−0.0292501
7	0.23918(85)	0.229154	0.27107(99)	0.261547
1-Body subtracted				
0	−0.42515(22)	−0.418321	−0.22082(77)	−0.209597
1	−0.4427(16)	−0.420459	−0.22082(77)	−0.209597
2	−0.42515(22)	−0.418321	−0.2105(10)	−0.21426
3	−0.20467(92)	−0.205913	−0.003783(77)	−0.000725653
4	−0.009048(21)	−0.00497328	−0.00841(12)	−0.00712178
5	−0.01640(23)	−0.014303	−0.00841(12)	−0.00712178
6	−0.009048(21)	−0.00497328	−0.003783(77)	−0.000725653
7	−0.20467(92)	−0.205913	−0.2105(10)	−0.21426
2-Body subtracted				
0	0.50834(19)	0.501635	0.49244(61)	0.492946
1	1.0275(13)	1.03178	0.49244(61)	0.492946
2	0.50834(19)	0.501635	0.00088(82)	−0.00837237
3	0.00966(69)	0.00184607	0.01489(11)	0.0147168
4	0.01936(10)	0.0168098	0.004382(45)	0.00071903
5	0.008576(91)	0.00141658	0.004382(45)	0.00071903
6	0.01936(10)	0.0168098	0.01489(11)	0.0147168
7	0.00966(69)	0.00184607	0.00088(82)	−0.00837237

in lattice units. Similarly, the radius of the energy density in the electric field can be computed as

$$\langle r^2\rangle_{E^2} = 0.33(15)\,. \tag{E6}$$

While there appears to be a large difference between these two radii, one must keep in mind that they are derived by weighting with distances that are constrained by the lattice spacing, or half-lattice spacing, and presently unquantified discretization effects are expected to be significant in these quantities. Further calculations at a smaller lattice spacing are

TABLE VIII. Measured and exact expectation values for the vacuum local charge density and energy in the electric field as shown in Fig. 10 (with zero external static charges). The uncertainties on measured values represent statistical fluctuations over the last ten wave functions of the VQE iterations and do not include estimates of associated systematic uncertainties. Note, from Table IV, that parity and translation invariance have been enforced.

r	$\langle\rho\rangle$	$\langle\rho\rangle_{\text{exact}}$	$\langle E^2\rangle$	$\langle E^2\rangle_{\text{exact}}$
GS probabilities associated with vacuum				
0-7	0.168677(14)	0.172982	0.0846006(74)	0.0866971

required to perform an extrapolation to the continuum limit and to provide a complete quantification of uncertainties.

It is interesting to note that there are static-charge configurations, such as the three-body $QQ\bar{Q}$ system at locations (0, 4, 1), that do not allow reduction of the Hilbert space through symmetry projections. It is this system in particular that has required the largest Hilbert space (68 dimensions) to achieve 1% precision on the ground-state energy used in the calculation of the corresponding three-body potential. While these symmetry projections have been critical for constructing systems with a dimension manageable with current quantum hardware and for removing dynamically irrelevant sectors from the perspective of the ground-state properties, it is interesting to note that knowledge of the symmetry properties without explicit projection could be used to probe systematic errors or noise within the quantum computation. For example, the local expectation values of the charge density and energy in the electric field shown in Fig. 9 for the (0, 2, 1) $QQ\bar{Q}$ system are currently forced theoretically to satisfy the parity projection through fermion site 1. If the 67-dimensional system (that before parity projection) was instead implemented by the QFP, deviations from this exact spatial symmetry would be indicative of the systematic uncertainty in the structure of the ground-state wave function.

APPENDIX F: CALCULATED VALUES

In this section, we present the values of local probabilities in the ground state (GS) of the vacuum, a single static charge, and two- and three-static-charge systems, that are shown in Figs. 9, 10, and Fig. 4 in the main text. Table VI contains the measured and exact expectation values of the local charge density and energy in the electric field with two static charges located at $r = 0, 2$, as shown in Fig. 4 of the main text. Table VII contains the same quantities for three static charges located at $r = 0, 1, 2$, as shown in Fig. 9. Table VIII contains the measured and exact expectation values for the vacuum local charge density and energy in the electric field as shown in Fig. 10. Table IX contains the same quantities for one static charge located at $r = 0$, as shown in Fig. 10.

TABLE IX. Measured and exact expectation values for the local charge density and energy in the electric field as shown in Fig. 10, with one static charge located at site zero. The uncertainties on measured values represent statistical fluctuations over the last ten wave functions of the VQE iterations and do not include estimates of associated systematic uncertainties. Note, from Table IV, that parity has been enforced for this system, leading to spatially symmetric locations having the same values.

r	$\langle\rho\rangle$	$\langle\rho\rangle_{\text{exact}}$	$\langle E^2\rangle$	$\langle E^2\rangle_{\text{exact}}$
GS probabilities associated with one static charge, at $r = 0$				
0	0.176000(24)	0.174705	0.588000(12)	0.587352
1	0.615612(14)	0.616012	0.0346655(84)	0.0351434
2	0.140169(14)	0.141965	0.112730(12)	0.113403
3	0.194102(24)	0.196036	0.082055(12)	0.0830207
4	0.163090(23)	0.165461	0.082055(12)	0.0830207
5	0.194102(24)	0.196036	0.112730(12)	0.113403
6	0.140169(14)	0.141965	0.0346655(84)	0.0351434
7	0.615612(14)	0.616012	0.588000(12)	0.587352
Vacuum subtracted				
0	0.007323(37)	0.00172308	0.503399(19)	0.500655
1	0.446935(26)	0.44303	−0.049935(15)	−0.0515537
2	−0.028508(25)	−0.0310171	0.028130(18)	0.0267057
3	0.025425(33)	0.0230541	−0.002545(17)	−0.0036764
4	−0.005587(30)	−0.00752077	−0.002545(17)	−0.0036764
5	0.025425(33)	0.0230541	0.028130(18)	0.0267057
6	−0.028508(25)	−0.0310171	−0.049935(15)	−0.0515537
7	0.446935(26)	0.44303	0.503399(19)	0.500655

[1] B. P. Lanyon, J. D. Whitfield, G. G. Gillett, M. E. Goggin, M. P. Almeida, I. Kassal, J. D. Biamonte, M. Mohseni, B. J. Powell, M. Barbieri *et al.*, Towards quantum chemistry on a quantum computer, Nat. Chem. **2**, 106 (2010).

[2] A. Peruzzo, J. McClean, P. Shadbolt, M.-H. Yung, X.-Q. Zhou, P. J. Love, A. Aspuru-Guzik, and J. L. O'Brien, A variational eigenvalue solver on a photonic quantum processor, Nat. Commun. **5**, 4213 (2014).

[3] R. Santagati, J. Wang, A. A. Gentile, S. Paesani, N. Wiebe, J. R. McClean, S. Morley-Short, P. J. Shadbolt, D. Bonneau, J. W. Silverstone, D. P. Tew, X. Zhou, J. L. O'Brien, and M. G. Thompson, Witnessing eigenstates for quantum simulation of Hamiltonian spectra, Sci. Adv. **4**, eaap9646 (2018).

[4] J. Huh, G. G. Guerreschi, B. Peropadre, J. R. McClean, and A. Aspuru-Guzik, Boson sampling for molecular vibronic spectra, Nat. Photon. **9**, 615 (2015).

[5] C. Sparrow, E. Martín-López, N. Maraviglia, A. Neville, C. Harrold, J. Carolan, Y. N. Joglekar, T. Hashimoto, N. Matsuda, J. L. O'Brien *et al.*, Simulating the vibrational quantum dynamics of molecules using photonics, Nature (London) **557**, 660 (2018).

[6] J. Wang, S. Paesani, R. Santagati, S. Knauer, A. A. Gentile, N. Wiebe, M. Petruzzella, J. L. O'Brien, J. G. Rarity, A. Laing *et al.*, Experimental quantum Hamiltonian learning, Nat. Phys. **13**, 551 (2017).

[7] P. Kok, W. J. Munro, K. Nemoto, T. C. Ralph, J. P. Dowling, and G. J. Milburn, Linear optical quantum

computing with photonic qubits, Rev. Mod. Phys. **79**, 135 (2007).

[8] A. Crespi, R. Ramponi, R. Osellame, L. Sansoni, I. Bongioanni, F. Sciarrino, G. Vallone, and P. Mataloni, Integrated photonic quantum gates for polarization qubits, Nat. Commun. **2**, 566 (2011).

[9] P. C. Humphreys, B. J. Metcalf, J. B. Spring, M. Moore, X.-M. Jin, M. Barbieri, W. S. Kolthammer, and I. A. Walmsley, Linear Optical Quantum Computing in a Single Spatial Mode, Phys. Rev. Lett. **111**, 150501 (2013).

[10] V. Ansari, J. M. Donohue, B. Brecht, and C. Silberhorn, Tailoring nonlinear processes for quantum optics with pulsed temporal-mode encodings, Optica **5**, 534 (2018).

[11] N. C. Harris, G. R. Steinbrecher, M. Prabhu, Y. Lahini, J. Mower, D. Bunandar, C. Chen, F. N. C. Wong, T. Baehr-Jones, M. Hochberg *et al.*, Quantum transport simulations in a programmable nanophotonic processor, Nat. Photon. **11**, 447 (2017).

[12] J. Wang, S. Paesani, Y. Ding, R. Santagati, P. Skrzypczyk, A. Salavrakos, J. Tura, R. Augusiak, L. Mančinska, D. Bacco, D. Bonneau, J. W. Silverstone, Q. Gong, A. Acín, K. Rottwitt, L. K. Oxenløwe, J. L. O'Brien, A. Laing, and M. G. Thompson, Multidimensional quantum entanglement with large-scale integrated optics, Science **360**, 285 (2018).

[13] X. Qiang, X. Zhou, J. Wang, C. M. Wilkes, T. Loke, S. O'Gara, L. Kling, G. D. Marshall, R. Santagati, T. C. Ralph *et al.*, Large-scale silicon quantum photonics implementing arbitrary two-qubit processing, Nat. Photon. **12**, 534 (2018).

[14] J. M. Lukens and P. Lougovski, Frequency-encoded photonic qubits for scalable quantum information processing, Optica **4**, 8 (2017).

[15] H.-H. Lu, J. M. Lukens, N. A. Peters, O. D. Odele, D. E. Leaird, A. M. Weiner, and P. Lougovski, Electro-Optic Frequency Beam Splitters and Tritters for High-Fidelity Photonic Quantum Information Processing, Phys. Rev. Lett. **120**, 030502 (2018).

[16] H.-H. Lu, J. M Lukens, N. A Peters, B. P. Williams, A. M. Weiner, and P. Lougovski, Controllable two-photon interference with versatile quantum frequency processor, Optica **5**, 1455 (2018).

[17] H.-H. Lu, J. M. Lukens, B. P. Williams, P. Imany, N. A. Peters, A. M. Weiner, and P. Lougovski, A controlled-NOT gate for frequency-bin qubits, npj Quantum Inf. **5**, 24 (2019).

[18] P. J. J. O'Malley, R. Babbush, I. D. Kivlichan, J. Romero, J. R. McClean, R. Barends, J. Kelly, P. Roushan, A. Tranter, N. Ding, B. Campbell, Y. Chen, Z. Chen, B. Chiaro, A. Dunsworth, A. G. Fowler, E. Jeffrey, E. Lucero, A. Megrant, J. Y. Mutus *et al.*, Scalable Quantum Simulation of Molecular Energies, Phys. Rev. X **6**, 031007 (2016).

[19] A. Kandala, A. Mezzacapo, K. Temme, M. Takita, M. Brink, J. M. Chow, and J. M. Gambetta, Hardware-efficient variational quantum eigensolver for small molecules and quantum magnets, Nature (London) **549**, 242 (2017).

[20] E. F. Dumitrescu, A. J. McCaskey, G. Hagen, G. R. Jansen, T. D. Morris, T. Papenbrock, R. C. Pooser, D. J. Dean, and P. Lougovski, Cloud Quantum Computing of an Atomic Nucleus, Phys. Rev. Lett. **120**, 210501 (2018).

[21] N. Klco, E. F. Dumitrescu, A. J. McCaskey, T. D. Morris, R. C. Pooser, M. Sanz, E. Solano, P. Lougovski, and M. J. Savage, Quantum-classical computation of Schwinger model dynamics using quantum computers, Phys. Rev. A **98**, 032331 (2018).

[22] H. Lamm and S. Lawrence, Simulation of Nonequilibrium Dynamics on a Quantum Computer, Phys. Rev. Lett. **121**, 170501 (2018).

[23] E. A. Martinez, C. A. Muschik, P. Schindler, D. Nigg, A. Erhard, M. Heyl, P. Hauke, M. Dalmonte, T. Monz, P. Zoller, and R. Blatt, Real-time dynamics of lattice gauge theories with a few-qubit quantum computer, Nature (London) **534**, 516 (2016).

[24] J. Zhang, G. Pagano, P. W. Hess, A. Kyprianidis, P. Becker, H. Kaplan, A. V. Gorshkov, Z.-X. Gong, and C. Monroe, Observation of a many-body dynamical phase transition with a 53-qubit quantum simulator, Nature (London) **551**, 601 (2017).

[25] C. Kokail, C. Maier, R. van Bijnen, R. Brydges, M. K. Joshi, P. Jurcevic, C. A. Muschik, P. Silvi, R. Blatt, C. F. Roos, and P. Zoller, Self-verifying variational quantum simulation of the lattice Schwinger model, Nature (London) **569**, 355 (2019).

[26] T. Yamazaki, Y. Kuramashi, and A. Ukawa (PACS-CS Collaboration), Helium nuclei in quenched lattice QCD, Phys. Rev. D **81**, 111504(R) (2010).

[27] S. R. Beane, E. Chang, W. Detmold, H. W. Lin, T. C. Luu, K. Orginos, A. Parreno, M. J. Savage, A. Torok, and A. Walker-Loud (NPLQCD Collaboration), The deuteron and exotic two-body bound states from lattice QCD, Phys. Rev. D **85**, 054511 (2012).

[28] N. Barnea, L. Contessi, D. Gazit, F. Pederiva, and U. van Kolck, Effective Field Theory for Lattice Nuclei, Phys. Rev. Lett. **114**, 052501 (2015).

[29] S. R. Beane, E. Chang, S. D. Cohen, W. Detmold, H. W. Lin, T. C. Luu, K. Orginos, A. Parreno, M. J. Savage, and A. Walker-Loud (NPLQCD Collaboration), Hyperon-Nucleon Interactions and the Composition of Dense Nuclear Matter from Quantum Chromodynamics, Phys. Rev. Lett. **109**, 172001 (2012), .

[30] S. R. Beane, E. Chang, S. D. Cohen, W. Detmold, H. W. Lin, T. C. Luu, K. Orginos, A. Parreno, M. J. Savage, and A. Walker-Loud (NPLQCD Collaboration), Light nuclei and hypernuclei from quantum chromodynamics in the limit of SU(3) flavor symmetry, Phys. Rev. D **87**, 034506 (2013).

[31] T. Yamazaki, Ken-ichi Ishikawa, Y. Kuramashi, and A. Ukawa, Helium nuclei, deuteron and dineutron in 2+1 flavor lattice QCD, Phys. Rev. D **86**, 074514 (2012).

[32] T. Inoue, S. Aoki, B. Charron, T. Doi, T. Hatsuda, Y. Ikeda, N. Ishii, K. Murano, H. Nemura, and K. Sasaki (HAL QCD Collaboration), Medium-heavy nuclei from nucleon-nucleon interactions in lattice QCD, Phys. Rev. C **91**, 011001(R) (2015).

[33] T. Yamazaki, Ken-ichi Ishikawa, Y. Kuramashi, and A. Ukawa, Study of quark mass dependence of binding energy for light nuclei in 2+1 flavor lattice QCD, Phys. Rev. D **92**, 014501 (2015).

[34] J. Kirscher, N. Barnea, D. Gazit, F. Pederiva, and U. van Kolck, Spectra and scattering of light lattice nuclei from effective field theory, Phys. Rev. C **92**, 054002 (2015).

[35] L. Contessi, A. Lovato, F. Pederiva, A. Roggero, J. Kirscher, and U. van Kolck, Ground-state properties of ^{4}He and ^{16}O extrapolated from lattice QCD with pionless EFT, Phys. Lett. B **772**, 839 (2017).

[36] A. Bansal, S. Binder, A. Ekström, G. Hagen, G. R. Jansen, and T. Papenbrock, Pion-less effective field theory for atomic nuclei and lattice nuclei, Phys. Rev. C **98**, 054301 (2018).

[37] T. Iritani, S. Aoki, T. Doi, S. Gongyo, T. Hatsuda, Y. Ikeda, T. Inoue, N. Ishii, H. Nemura, and K. Sasaki (HAL QCD

Collaboration), Systematics of the HAL QCD potential at low energies in lattice QCD, Phys. Rev. D **99**, 014514 (2019).
[38] P. F. Bedaque and U. van Kolck, Effective field theory for few-nucleon systems, Annu. Rev. Nucl. Part. Sci. **52**, 339 (2002).
[39] E. Epelbaum, H.-W. Hammer, and U.-G. Meißner, Modern theory of nuclear forces, Rev. Mod. Phys. **81**, 1773 (2009).
[40] R. Machleidt and D. R. Entem, Chiral effective field theory and nuclear forces, Phys. Rep. **503**, 1 (2011).
[41] P. Navrátil, S. Quaglioni, I. Stetcu, and B. R. Barrett, Recent developments in no-core shell-model calculations, J. Phys. G: Nucl. Part. Phys. **36**, 083101 (2009).
[42] B. R. Barrett, P. Navrátil, and J. P. Vary, *Ab initio* no core shell model, Prog. Part. Nucl. Phys. **69**, 131 (2013).
[43] G. Hagen, A. Ekström, C. Forssén, G. R. Jansen, W. Nazarewicz, T. Papenbrock, K. A. Wendt, S. Bacca, N. Barnea, B. Carlsson, C. Drischler, K. Hebeler, M. Hjorth-Jensen, M. Miorelli, G. Orlandini, A. Schwenk, and J. Simonis, Neutron and weak-charge distributions of the ^{48}Ca nucleus, Nat. Phys. **12**, 186 (2016).
[44] T. D. Morris, J. Simonis, S. R. Stroberg, C. Stumpf, G. Hagen, J. D. Holt, G. R. Jansen, T. Papenbrock, R. Roth, and A. Schwenk, Structure of the Lightest Tin Isotopes, Phys. Rev. Lett. **120**, 152503 (2018).
[45] G. Parisi, The strategy for computing the hadronic mass spectrum, Phys. Rep. **103**, 203 (1984).
[46] G. P. Lepage, The analysis of algorithms for lattice field theory, in *Boulder ASI 1989:97-120* (1989), pp. 97–120, https://lib-extopc.kek.jp/preprints/PDF/1990/9003/9003479.pdf.
[47] S. R. Beane, W. Detmold, T. C Luu, K. Orginos, A. Parreno, M. J. Savage, A. Torok, and A. Walker-Loud, High statistics analysis using anisotropic clover lattices, II. Three-baryon systems, Phys. Rev. D **80**, 074501 (2009).
[48] S. R. Beane, W. Detmold, T. C. Luu, K. Orginos, A. Parreno, M. J. Savage, A. Torok, and A. Walker-Loud (NPLQCD Collaboration), High statistics analysis using anisotropic clover lattices, I. Single hadron correlation functions, Phys. Rev. D **79**, 114502 (2009).
[49] M. L. Wagman and M. J. Savage, Statistics of baryon correlation functions in lattice QCD, Phys. Rev. D **96**, 114508 (2017).
[50] E. Ovrum and M. Hjorth-Jensen, Quantum computation algorithm for many-body studies, arXiv:0705.1928.
[51] S. P. Jordan, K. S. M. Lee, and J. Preskill, Quantum algorithms for quantum field theories, Science **336**, 1130 (2012).
[52] S. P. Jordan, K. S. M. Lee, and J. Preskill, Quantum computation of scattering in scalar quantum field theories, Quantum Inf. Comput. **14**, 1014 (2014).
[53] K. Marshall, R. Pooser, G. Siopsis, and C. Weedbrook, Quantum simulation of quantum field theory using continuous variables, Phys. Rev. A **92**, 063825 (2015).
[54] L. Olislager, J. Cussey, A. T. Nguyen, P. Emplit, S. Massar, J.-M. Merolla, and K. P. Huy, Frequency-bin entangled photons, Phys. Rev. A **82**, 013804 (2010).
[55] Significant technical challenges remain in demonstrating entangling operations in a space of this size.
[56] J. R. McClean, J. Romero, R. Babbush, and A. Aspuru-Guzik, The theory of variational hybrid quantum-classical algorithms, New J. Phys. **18**, 023023 (2016).
[57] D. A. Mazziotti, Anti-Hermitian Contracted Schrödinger Equation: Direct Determination of the Two-Electron Reduced Density Matrices of Many-Electron Molecules, Phys. Rev. Lett. **97**, 143002 (2006).
[58] T. D. Morris, Improved optimization of unitary coupled cluster ansatz (unpublished).
[59] R. Fletcher, *Practical Methods of Optimization* (Wiley, New York, 1987).
[60] D. B. Kaplan, M. J. Savage, and M. B. Wise, Two nucleon systems from effective field theory, Nucl. Phys. B **534**, 329 (1998).
[61] U. van Kolck, Effective field theory of short range forces, Nucl. Phys. A **645**, 273 (1999).
[62] D. B. Kaplan, M. J. Savage, and M. B. Wise, A new expansion for nucleon-nucleon interactions, Phys. Lett. B **424**, 390 (1998).
[63] P. F. Bedaque, H.-W. Hammer, and U. van Kolck, Renormalization of the Three-Body System with Short-Range Interactions, Phys. Rev. Lett. **82**, 463 (1999).
[64] J. C. Light and T. Carrington, Discrete-variable representations and their utilization, in *Advances in Chemical Physics*, edited by I. Prigogine and S. A. Rice (John Wiley & Sons, New York, 2007), pp. 263–310.
[65] J. S. Schwinger, Gauge invariance and mass. II, Phys. Rev. **128**, 2425 (1962).
[66] S. R. Coleman, R. Jackiw, and L. Susskind, Charge shielding and quark confinement in the massive Schwinger model, Ann. Phys. **93**, 267 (1975).
[67] J. Potvin, A nonperturbative study of hadronization with heavy sources: The screening length as a function of the quark mass in the Schwinger model, Phys. Rev. D **32**, 2070 (1985).
[68] M. C. Banuls, K. Cichy, K. Jansen, and J. I. Cirac, The mass spectrum of the Schwinger model with matrix product states, J. High Energy Phys. 11 (2013) 158.
[69] Y. Shimizu and Y. Kuramashi, Critical behavior of the lattice Schwinger model with a topological term at $\theta = \pi$ using the Grassmann tensor renormalization group, Phys. Rev. D **90**, 074503 (2014).
[70] Y. Shimizu and Y. Kuramashi, Grassmann tensor renormalization group approach to one-flavor lattice Schwinger model, Phys. Rev. D **90**, 014508 (2014).
[71] M. C. Banuls, K. Cichy, J. I. Cirac, K. Jansen, and H. Saito, Thermal evolution of the Schwinger model with matrix product operators, Phys. Rev. D **92**, 034519 (2015).
[72] M. C. Bañuls, K. Cichy, K. Jansen, and H. Saito, Chiral condensate in the Schwinger model with matrix product operators, Phys. Rev. D **93**, 094512 (2016).
[73] M. C. Banuls, K. Cichy, J. I. Cirac, K. Jansen, and S. Kühn, Density Induced Phase Transitions in the Schwinger Model: A Study with Matrix Product States, Phys. Rev. Lett. **118**, 071601 (2017).
[74] B. Buyens, F. Verstraete, and K. Van Acoleyen, Hamiltonian simulation of the Schwinger model at finite temperature, Phys. Rev. D **94**, 085018 (2016).
[75] B. Buyens, J. Haegeman, F. Hebenstreit, F. Verstraete, and K. Van Acoleyen, Real-time simulation of the Schwinger effect with matrix product states, Phys. Rev. D **96**, 114501 (2017).
[76] J. B. Kogut and L. Susskind, Hamiltonian formulation of Wilson's lattice gauge theories, Phys. Rev. D **11**, 395 (1975).
[77] S. R. White, Numerical canonical transformation approach to quantum many-body problems, J. Chem. Phys. **117**, 7472 (2002).

[78] J. C. Light, I. P. Hamilton, and J. V. Lill, Generalized discrete variable approximation in quantum mechanics, J. Chem. Phys. **82**, 1400 (1985).

[79] D. Baye and P.-H. Heenen, Generalised meshes for quantum mechanical problems, J. Phys. A: Math. Gen. **19**, 2041 (1986).

[80] R. G. Littlejohn, M. Cargo, T. Carrington, K. A. Mitchell, and B. Poirier, A general framework for discrete variable representation basis sets, J. Chem. Phys. **116**, 8691 (2002).

[81] S. Binder, A. Ekström, G. Hagen, T. Papenbrock, and K. A. Wendt, Effective field theory in the harmonic oscillator basis, Phys. Rev. C **93**, 044332 (2016).

[82] R. Machleidt, High-precision, charge-dependent Bonn nucleon-nucleon potential, Phys. Rev. C **63**, 024001 (2001).

[83] P. Navrátil, G. P. Kamuntavičius, and B. R. Barrett, Few-nucleon systems in a translationally invariant harmonic oscillator basis, Phys. Rev. C **61**, 044001 (2000).

[84] P. Navrátil, Local three-nucleon interaction from chiral effective field theory, Few-Body Syst. **41**, 117 (2007).

[85] R. J. Furnstahl, G. Hagen, and T. Papenbrock, Corrections to nuclear energies and radii in finite oscillator spaces, Phys. Rev. C **86**, 031301(R) (2012).

[86] M. Lüscher, Volume dependence of the energy spectrum in massive quantum field theories. I. Stable particle states, Commun. Math. Phys. **104**, 177 (1986).

[87] M. Lüscher, Volume dependence of the energy spectrum in massive quantum field theories. II. Scattering states, Commun. Math. Phys. **105**, 153 (1986).

[88] S. König and D. Lee, Volume dependence of n-body bound states, Phys. Lett. B **779**, 9 (2018).

[89] C. Forssén, B. D. Carlsson, H. T. Johansson, D. Sääf, A. Bansal, G. Hagen, and T. Papenbrock, Large-scale exact diagonalizations reveal low-momentum scales of nuclei, Phys. Rev. C **97**, 034328 (2018).

[90] K. A. Wendt, C. Forssén, T. Papenbrock, and D. Sääf, Infrared length scale and extrapolations for the no-core shell model, Phys. Rev. C **91**, 061301(R) (2015).

[91] R. J. Furnstahl, S. N. More, and T. Papenbrock, Systematic expansion for infrared oscillator basis extrapolations, Phys. Rev. C **89**, 044301 (2014).

[92] J.-W. Chen, G. Rupak, and M. J. Savage, Nucleon-nucleon effective field theory without pions, Nucl. Phys. A **653**, 386 (1999).

[93] http://energy.gov/downloads/doe-public-access-plan.